Submarine back-arc lava with arc signature: Fonualei Spreading Center, northeast Lau Basin, Tonga

Nicole S. Keller,[1,2] Richard J. Arculus,[1] Jörg Hermann,[1] and Simon Richards[1,3]

[1]   We present major, volatile, and trace elements for quenched glasses from the Fonualei Spreading Center, a nascent spreading system situated very close to the Tofua Volcanic Arc (20 km at the closest), in the northeast Lau Basin. The glasses are basalts and basaltic andesites and are inferred to have originated from a relatively hot and depleted mantle wedge. The Fonualei Spreading Center shows island arc basalt (IAB) affinities, indistinguishable from the Tofua Arc. Within the Fonualei Spreading Center no geochemical trends can be seen with depth to the slab and/or distance to the arc, despite a difference in depth to the slab of >50 km. Therefore we infer that all the subduction-related magmatism is captured by the back arc as the adjacent arc is shut off. There is a sharp contrast between the main spreading area of the Fonualei Spreading Center (FSC) and its northernmost termination, the Mangatolu Triple Junction (MTJ). The MTJ samples are characteristic back-arc basin basalts (BABB). We propose that the MTJ and FSC have different mantle sources, reflecting different mantle origins and/or different melting processes. We also document a decrease in mantle depletion from the south of the FSC to the MTJ, which is the opposite to what has been documented for the rest of the Lau Basin where depletion generally increases from south to north. We attribute this reverse trend to the influx of less depleted mantle through the tear between the Australian and the Pacific plates, at the northern boundary of the Lau Basin.

1.   Introduction

[2]   Through study of the igneous crusts of back-arc basins we can obtain geochemical insights into subduction zone processes, and in particular, characteristics of the subarc mantle wedge and the subduction component thought to be linked to the melt generation process [e.g., *Tatsumi and Eggins*, 1995]. Furthermore, eruption in extensional settings reduces the complications inherent to arc magmatism where melt evolution may be affected by ascent through and interaction with crustal sequences typically thicker and more fusible than those in back arcs. Back-arc basins also tend to be dominated by mafic eruptives, whereas the larger, individual arc edifices are typically mantled by more silica-rich compositions, which render geochemical inversions for source compositions in the mantle wedge and subducted plate more difficult.

[3]   Early studies of back-arc basins led to the assumption that the generation of back-arc basin lavas was dominated by the same processes that control melting at mid-ocean ridges, based on their comparable compositional trends [e.g., *Hart et al.*, 1972]. Further studies revealed that mid-ocean ridge basalt (MORB)-type petrogenesis alone does not account for the geochemical systematics found in back arcs and that their geochemistry is transitional between MORB and island arc basalts (IAB) [*Gill*, 1976].

[4]   Back-arc basin basalt (BABB) was first explicitly described by *Fryer et al.* [1981] in a study of the Mariana Trough, wherein the major compositional differences between BABB and MORB were discussed. Subsequently, many studies of back-arc basins all over the world contributed to developing our understanding of the generation of BABB. Compilations of BABB major element systematics have recently been presented by *Taylor and Martinez* [2003] and *Langmuir et al.* [2006], whereas *Pearce and Stern* [2006] reviewed trace element abundances and isotopic systematics. As summarized by these authors, the petrogenesis of BABB can be accounted for by combinations of the following factors: (1) asthenospheric input into the mantle region that melts beneath the back arc; (2) subduction zone input into this same back-arc region of mantle melting; (3) mixing between factors 1 and 2; and (4), melting conditions and fractionation of the melt during its ascent to the ocean floor. This results in BABB that are transitional between MORB (dominated by decompression melting) and IAB (dominated by flux melting caused by the subduction input). They tend to have slightly higher SiO_2, Al_2O_3, and Na_2O than normal (N-)MORB and somewhat lower TiO_2,

[1]Research School of Earth Sciences, Australian National University, Canberra, ACT, Australia.
[2]Now at Geology and Geophysics Department, Woods Hole Oceanographic Institution, Woods Hole, Massachusetts, USA.
[3]Now at School of Earth Sciences, James Cook University, Townsville, Queensland, Australia.

FeO, and MgO [e.g., *Fryer et al.*, 1990; *Langmuir et al.*, 2006]. BABB are usually hydrous, containing up to 2.5 wt% H_2O [*Langmuir et al.*, 2006]; they show a notable enrichment in large ion lithophile elements (LILE), Sr and Pb, and depletion in high field strength elements (HFSE) relative to N-MORB [e.g., *Pearce and Stern*, 2006]. The enrichment features are attributed to the difference in water contents between MORB and IAB/BABB [*Stolper and Newman*, 1994] and generally referred to as the "subduction component" [e.g., *Tatsumi and Eggins*, 1995]. The nature of this component is still under debate, as it has been inferred to be either an aqueous phase or a (more or less) hydrous melt, depending on the local thermal structure of the subducting slab and the overlying mantle wedge [e.g., *Elliott et al.*, 1997; *Johnson and Plank*, 1999; *Hermann et al.*, 2006]. Regardless of its character, on a large scale (e.g., hundreds of kilometers) the subduction component generally decreases with increasing distance to the arc [*Stern et al.*, 1990; *Gribble et al.*, 1998; *Martinez and Taylor*, 2002; *Sinton et al.*, 2003; *Stern et al.*, 2006]. Consequently, spreading centers located relatively close to an arc tend to show a strong subduction signature and therefore help with studying the latter [e.g., *Fryer et al.*, 1990; *Gribble et al.*, 1998; *Fretzdorff et al.*, 2006]. The Fonualei Spreading Center, in northern Tonga, is significant in this regard as its southern tip lies within 20 km of the Tofua Arc. Furthermore, by studying a nascent back-arc basin we hope to shed some light on melting processes at the arc/back arc transition, as there has been some debate as to whether the initial melts generated at the onset of rifting are BABB (e.g., Sumisu Rift [*Fryer et al.*, 1990]) or IAB (e.g., Mariana Troughs [*Gribble et al.*, 1998]).

[5] We present here major, volatile, and trace elements for glassy rims of submarine samples dredged from the Fonualei Spreading Center and its northern termination, the Mangatolu Triple Junction. Glassy samples from lavas that erupted on the ocean floor offer the advantage of being less degassed than subaerial samples as the water pressure and the fast rate of quenching will limit pressure-driven volatile loss and chemical changes resulting from it. We evaluate our data with other sets published for the rest of the Lau Basin together with other back arcs. Given the proximity of the Fonualei Spreading Center to the fastest converging subduction zone on Earth [*Bevis et al.*, 1995], the samples dredged from the Fonualei Spreading Center provide a unique insight into the processes involved in mantle melting in subduction environments.

2. Geological Settings

2.1. Tonga-Kermadec Subduction System

[6] The Tonga-Kermadec subduction system is a zone of major intraoceanic plate convergence in the southwest Pacific, extending in a NNE direction from the Taupo Volcanic Zone (TVZ) on the North Island of New Zealand to the south of Samoa, with a total length of 2800 km (Figure 1). Subduction of the Pacific Plate beneath the Indo-Australian Plate has resulted in the formation of a volcanic arc and associated back-arc basins. The southernmost active volcano of the arc in the TVZ is Mt. Ruapehu; the northernmost subaerial volcano is the island of Tafahi at the northern tip of the Tongan archipelago. In between these two volcanoes are >80 submarine and subaerial volcanic centers [*de Ronde et al.*, 2001; *Arculus et al.*, 2003; *de Ronde et al.*, 2003; *Arculus*, 2004; *Stoffers et al.*, 2006; *Wright et al.*, 2006]. To the west of the trench lies a zone of crustal extension: in the south, the TVZ; further north, the Havre Trough west of the Kermadec Islands, and in the north, the Lau Basin, west of the Tonga Islands. The subduction rate increases from south to north, reaching 240 mm a^{-1} in the northernmost part [*Bevis et al.*, 1995], where the Tonga Trench reaches a depth of approximately 9000 m [*Wright et al.*, 2000]. This is the locus of the fastest plate convergence on Earth, giving rise to anomalously high seismicity [e.g., *Zheng et al.*, 2007].

2.2. Lau Basin

[7] The Lau Basin is shown in Figure 1. It is a triangular depression over 1000 km long and approximately 450 km wide in the north (15°S), narrowing to about 200 km in the south (25°S). This active back-arc basin has been opening over the last 6 Ma [*Hawkins*, 1995] through rapid clockwise rotation (7°/Ma) of the Tonga Arc; the Euler pole of the motion lies around 24°S [*Bevis et al.*, 1995]. The basin is bordered to the east by the Tonga Ridge and to the west by the Lau Ridge. The Tonga Arc is a double island chain: the eastern chain, lying 130 to 150 km west of the trench, consists of islands which are mostly limestone covered and no longer active. The western chain (referred to as the Tofua Arc) comprises several dozen active and dormant, subaerial and submarine volcanic edifices, and lies 150–200 km west of the Tonga Trench. The most active subaerial volcanoes of the Tofua Arc are Tofua, Late, and Fonualei, all of which have historical eruptions. Several (mostly) submarine volcanoes such as Metis Shoal and Home Reef erupt episodically and form ephemeral islands. The Lau Ridge is a remnant volcanic arc abandoned by spreading in the Lau Basin, and was active between the mid-Miocene and early Pliocene (approximately 15–5 Ma [*Hawkins*, 1995]).

[8] The Lau Basin comprises a series of mainly south to southwest propagating rift axes (the notable exceptions being the Lau Extensional Transform Zone (LETZ) and Peggy Ridge (PR) which are oriented northwest to southeast). The most prominent spreading zones are the Eastern Lau Spreading Center (ELSC), with its southern propagator, the Valu Fa Ridge (VFR); north of the ELSC, the Central Lau Spreading Center (CLSC); the Intermediate Lau Spreading Center (ILSC) bridging the gap between ELSC and CLSC. To the northeast of the CLSC lies the Lau Extensional Transform Zone (LETZ) which merges into Peggy Ridge (PR) and the Northwest Lau Spreading Center (NWLSC) further to the west. Northeast of the ELSC, the Fonualei Spreading Center (FSC) extends from the subaerial volcano Fonualei to the Mangatolu Triple Junction (MTJ), also known as the King's Triple Junction (KTJ). Northwest of the MTJ lies the North East Lau Spreading Center (NELSC), and in the northernmost part of the basin, the Niuafo'ou Spreading Center (NSC) striking NE–SW, joining the NWLSC in the southwest. *Zellmer and Taylor* [2001] proposed that the Lau Basin is composed of three plates, the Australian Plate in the west, bordered on the east by the VFR, ELSC, CLSC, LETZ, and PR; the Tonga Plate on the east, bordered on the west by the FSC and the Tonga Trench on the east; and the aseismic Niuafo'ou Microplate
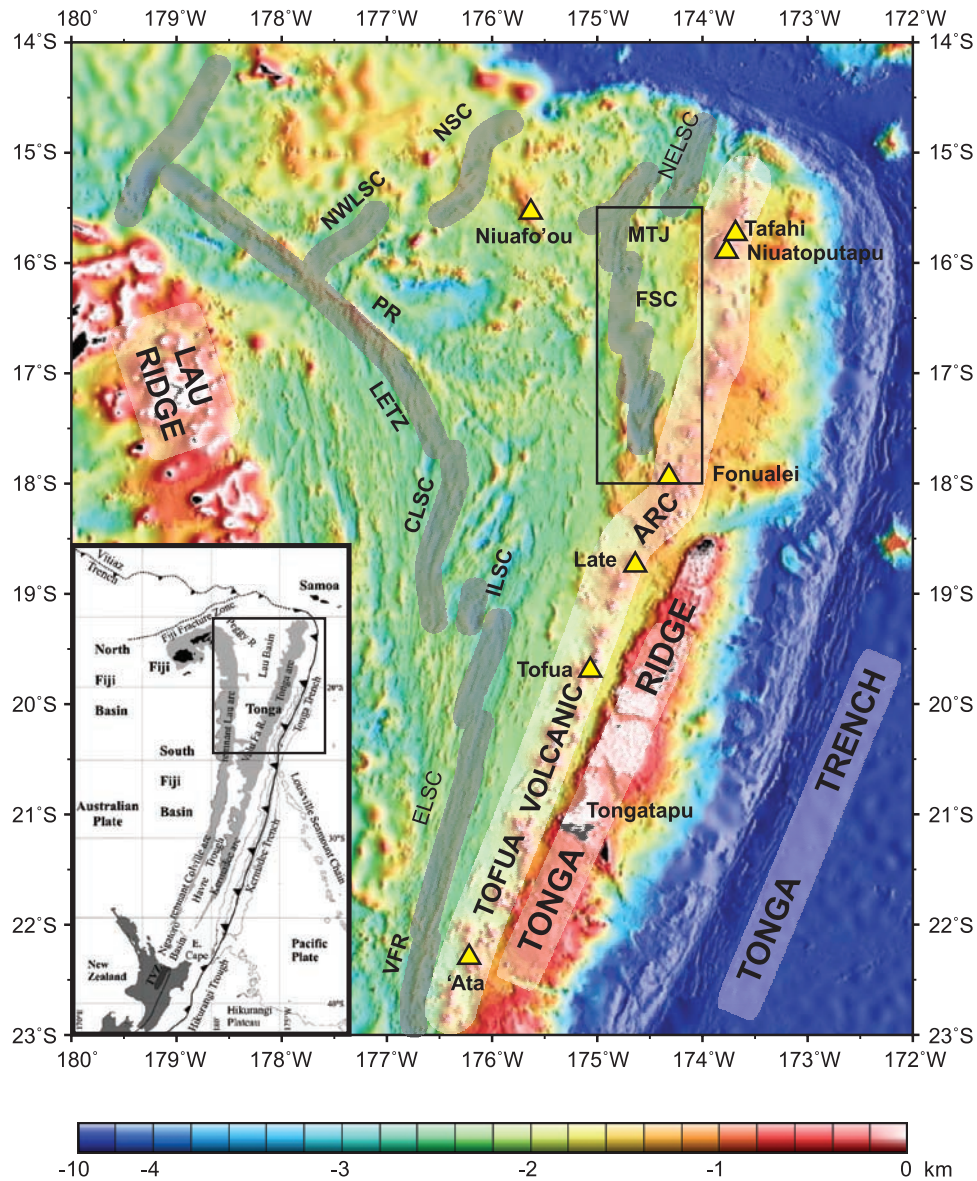
Figure 1. Bathymetric map of the Lau Basin, showing the main spreading centers [after *Zellmer and Taylor*, 2001], geographical features, and subaerial volcanoes (yellow triangles). VFR, Valu Fa Ridge; ELSC, East Lau Spreading Center; ILSC, Intermediate Lau Spreading Center; CLSC, Central Lau Spreading Center; LETZ, Lau Extentional Transform Zone; PR, Peggy Ridge; NWLSC, Northwest Lau Spreading Center; NSC, Niuafo'ou Spreading Center; NELSC, Northeast Lau Spreading Center; FSC, Fonualei Spreading Center; MTJ, Mangatolu Triple Junction. The black rectangle shows the area of this study, shown in more detail in Figure 3. Yellow triangles indicate subaerial volcanoes. Insert shows a regional tectonic map of the Tonga-Kermadec subduction system, from *Smith and Price* [2006] with permission from Elsevier.

in between [see *Zellmer and Taylor*, 2001, Figure 6]. The only subaerial back-arc volcano of the Lau Basin, Niuafo'ou, is situated on the microplate of the same name, between the MTJ and the NSC. The northern termination of the Lau Basin is determined by the Fiji fracture zone, a strike-slip fault that forms the boundary between the Tonga and Niuafo'ou plates in the south and the Pacific Plate in the north [*Hamburger and Isacks*, 1988]. *Millen and Hamburger* [1998] showed seismic evidence of tearing of the Pacific Plate at the northern end of the basin, which has also been

inferred from geochemical studies of the area [e.g., *Turner and Hawkesworth*, 1997].

[9] The geochemistry of the oceanic crust in the Lau Basin is consistent with MORB-type melt generation, albeit relatively depleted due to a long history of melting (summarized by *Hawkins* [1995]). It is also influenced by the subduction processes and the enhancement of the subduction signature (e.g., high LILE, low HFSE) with proximity to the arc has been well documented [e.g., *Pearce et al.*, 1995; *Taylor and Martinez*, 2003].
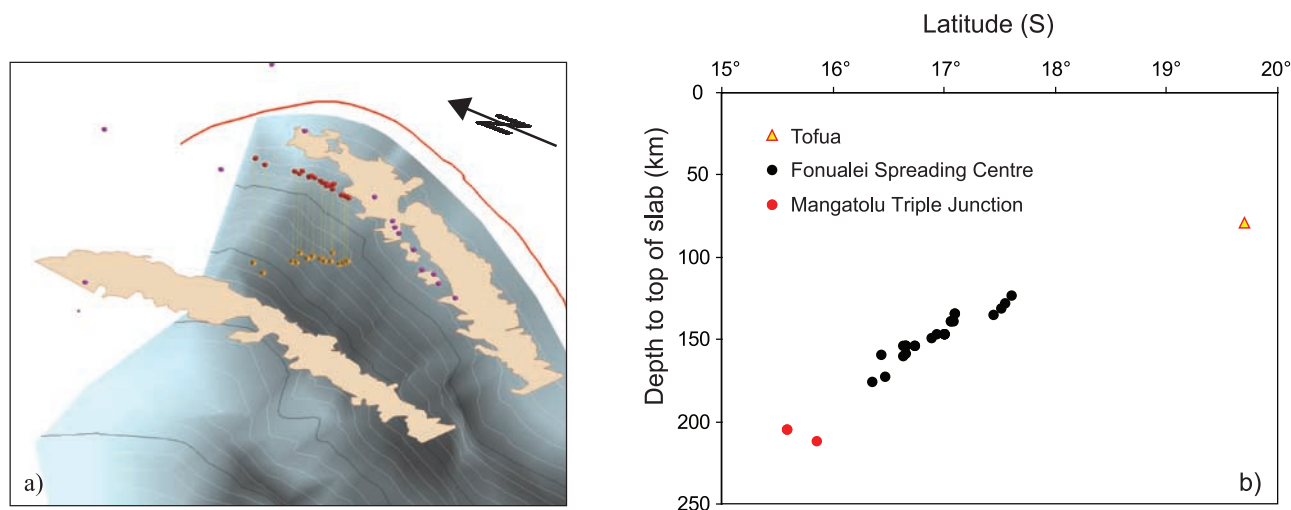
Figure 2. (a) Three-dimensional reconstruction of the upper surface of the Pacific Plate dipping below Tonga. Beige areas represent the Lau Ridge on the left and the Tonga Ridge on the right, using a 1500 m bathymetry contour from *Zellmer and Taylor* [2001]. Purple dots indicate subaerial volcanoes (locations from the NGDC catalog). The red line indicates the outer boundary of the Australian Plate. Red dots indicate sample locations along the Fonualei Spreading Center, with their corresponding vertical tie line showing the intersection with the slab surface with an orange cube. The length of these tie lines gives the depth to the slab for each point. White contours on the slab indicate 20 km equilines, whereas black contours correspond to 100 km intervals. (b) Depth to the top of the subducting slab for each sample location.

2.3. Fonualei Spreading Center

[10] Compared to the southern and central parts of the Lau Basin, the northeastern part has so far received relatively little attention, and to this date only few publications mention the spreading center located between the island of Fonualei and the Mangatolu Triple Junction [*Zellmer and Taylor*, 2001; *German et al.*, 2006]. The Fonualei Spreading Center is located to the north of the active volcano Fonualei (Figure 1). It is an actively spreading system, consisting of north-northeast, south-southwest trending ridges, volcanic centers generally located on top of the ridges, and deeper basins. The ridges have an en échelon geometry, extending from the MTJ in the north (120 km distant from the Tofua Arc) to the south where the Fonualei Spreading Center is most proximal to the Tofua Arc (20 km). The Fonualei Spreading Center was recognized by *Zellmer and Taylor* [2001] to be the boundary between the Tonga Plate and the Niuafo'ou Microplate. These authors estimate spreading rates increasing from 47 mm a^{-1} in the south to 94 mm a^{-1} in the north. In previous publications [*Zellmer and Taylor*, 2001; *German et al.*, 2006] this spreading center was referred to as the Fonualei Rifts and Spreading Center (FRSC). However, given the relatively high spreading rate and the absence of felsic lavas, it is more likely that the system is already at a spreading stage, rather than rifting, thus we adopt the denomination of Fonualei Spreading Center (FSC).

2.4. Geometry of the Tonga Slab

[11] Because the strike of the FSC is not parallel to the Tonga trench, the depth to the slab of the spreading system increases from south to north. This may result in changes in the temperature and pressure distribution vertically below

the FSC, affecting processes taking place at the top of the slab (such as melt and/or aqueous fluid release), which in turn might influence the geochemistry of the eruptive products. In order to assess whether such effects can be seen on the scale of an individual spreading system, a study of the variation of elements and element ratios as a function of depth to the slab was conducted. This requires precise knowledge of the depth to the slab for individual sample locations, which can be achieved by digital reconstruction of the subduction system. The details of our approach can be found in Appendix A. Figure 2a shows the interpreted 3-D geometry of the Pacific Plate at the Tonga subduction zone. Our reconstruction shows that the depth to the slab increases approximately linearly with decreasing latitude, as can be seen in Figure 2b. The depth to the slab for each sample location can be found in Table 1.

3. Sample Collection, Preparation, and Analysis

3.1. Sampling

[12] Our study of the FSC used submarine glass samples dredged during a research voyage (SS11/04) of the Australian Marine National Facility (R/V *Southern Surveyor*) in 2004 (also known as Northern Tonga Vents Expedition (NoToVE)). The primary aims of NoToVE, complementing previous voyages in the Kermadec (NZAPLUMEI to III) and southern Tonga (TELVE) regions, were to study the submarine volcanism and hydrothermalism of the northernmost segment of the Tofua Arc and adjacent FSC. Bathymetry and acoustic backscatter were obtained with a multibeam sonar swath system (30 kHz; EM300), while dredging and hydrocasting were used to recover rock and water samples, respectively. Figure 3a presents a bathymetric map of the FSC produced during NoToVE and

Table 1. Dredge Locations and Description of Samples Recovered From the Fonualei Spreading Centre During Cruise NoToVE, R/V *Southern Surveyor*

Sample ID	Description of Dredge Target	Latitude (°S)	Longitude (°W)	Water Depth (m)	Depth to Slab (km)[a]	Macroscopic Description of Dredge Haul	Phenocrysts in Glassy Rim[b]	Vesicularity (%)
Fonualei Spreading Centre South (FSC S)								
47.1	Cone on propagator	17°38	174°34	2620	125	Black, glassy-rinded, moderately vesicular, plag-ol-microphyric basalt (flow exteriors and interiors).	ol, cr-sp	40
48.1	Rift flank	17°34	174°34	1690	129	Black, vesicular, ol-plag-phyric, glass-rinded pillow basalts.	plag, px (core zoned opx-cpx)	7
46.1	Flank of large cone on ridge	17°32	174°34	1340	132	Black, glass rinded, moderately vesicular to massive, aphyric volcanic rock.	plag, px (core zoned opx-cpx)	5
45.1	Cone on central ridge	17°28	174°35	1890	136	Black-grey, highly vesicular, glass-rinded, plag-ol-microphyric basalt with some degree of Fe-staining.	ol, plag, cpx, cr-sp	15
Fonualei Spreading Centre Central South (FSC CS)								
42.1	Central high on ridge	17°07	174°27	1310	136	Black, highly vesicular, glassy-encrusted pillow and flow exteriors of sparsely olivine-microphyric basalt.	ol, cr-sp	30
43.1	Medium size cone	17°07	174°25	1640	136	Black, thin vesicular glass encrusted pillows and flows of olivine-phyric basalt. Small amount of Fe-staining.	plag	10
40.1	Young lava flow, flank of large cone on central ridge	17°06	174°31	1670	140	Black, glassy rinded pillow exteriors and interiors of aphyric basalt.	plag, px (core zoned opx-cpx)	7
38.1	Medium size cone on central ridge	17°05	174°34	1880	140	Grey-black, massive to highly vesicular, pillow tops and interiors of very sparsely olivine-microphyric basalt.	ol, cr-sp	25
39.1	Young lava field west of central ridge	17°05	174°32	2170	140	Black, sparsely vesicular to massive, glassy flow tops and interiors of very sparsely ol-cpx microphyric basalt.	plag, px (core zoned opx-cpx)	0
37.1	Small cone on overlapper ridge	17°01	174°30	1600	148	Black, vesicular, olivine-microphyric pillow fragments with glass rinds. Light brown staining between glass rind and vesicular pillow interiors.	ol, plag, cpx, cr-sp	10
37.2	Small cone on overlapper ridge	17°01	174°30	1600	148	Black, sparsely vesicular, very sparsely olivine-cpx-microphyric glass-rinded flow tops and interior.	ol, plag, cpx	35
56.1	Cone	17°01	174°31	1520	148	Black fragments of vesicular basalt.	ol, px (core zoned opx-cpx), cr-sp	40
57.1	Cone (same as 56.1)	17°01	174°31	1540	148	Black, glass-encrusted pillow lava exteriors and interiors, ol-cpx-phyric.	px±core zoned opx-cpx)	50
34.1	Crest of ridge	16°57	174°32	1510	148	Black, slightly vesicular, sparsely olivine-microphyric basalt with glass rinded flow tops and glass chips.	plag, cpx	35
58.2	Flank of central ridge crest	16°54	174°31	1680	151	Glass chips from black, glass-encrusted, pillow lava exteriors/interiors (vesicular), cpx-plag -phyric basalt.	plag, cpx	35
Fonualei Spreading Centre Central North (FSC CN)								
60.1	Termination of central ridge crest	16°45	174°31	1840	155	Very fresh, black, glass-encrusted vesicular interiors of pillows and flows, green olivine-microphyric basalt.	plag, cpx, opx	15
60.2	Termination of central ridge crest	16°45	174°31	1840	155	Glass chips of above.	plag, cpx, opx	25

B08S07   KELLER ET AL.: GEOCHEMISTRY OF THE FONUALEI SPREADING CENTER   **B08S07**

Table 1. (continued)

Sample ID	Description of Dredge Target	Latitude (°S)	Longitude (°W)	Water Depth (m)	Depth to Slab (km)[a]	Macroscopic Description of Dredge Haul	Phenocrysts in Glassy Rim[b]	Vesicularity (%)
61.1	Termination of central ridge crest	16°4	174°31	1850	155	Black (black-green) glassy, variably vesicular, olivine-microphyric basalt.	sector zoned cpx,opx	35
61.2	Termination of central ridge crest	16°4	174°31	1850	155	Glass chips of above.	ol, cpx, opx, cr-sp	5
62.1	Summit of cone	16°4	174°33	1240	155	Black, thickly glass-encrusted, variably vesicular olivine-microphyric basalt.	plag, px (core zoned opx-cpx)	40
64.1	Flank of ridge	16°4	174°35	1690	160	Black, glass-encrusted, highly vesicular interiors, pillow rim fragments of basalt.	ol, cr-sp	25
63.1	Flank of wall in pull-apart basin	16°39	174°34	1730	162	Thickly black glass-encrusted pillow lava and lava tube flows, olivine-microphyric basalt.	plag, cpx, opx	0
63.2	Flank of wall in pull-apart basin	16°39	174°34	1730	162	Glass chips of above.	plag, cpx	5
Fonualei Spreading Centre North (FSC N)								
66.1	End of ridge segment	16°29	174°38	1720	175	Black, degraded glass-encrusted, variably vesicular basalt.	ol, cpx	35
68.1	Flank of cone structure	16°27	174°31	1750	161	Black, glass-encrusted variably vesicular, olivine-microphyric pillow fragments of basalt.	ol, cpx, cr-sp	20
67.3	End of ridge segment	16°22	174°37	1750	177	Fe-stained, black-grey, variably vesicular basalt.	plag, cpx	40
Mangatolu Triple Junction (MTJ)								
70.1	Axial ridge crest	15°52	174°51	2500	214	Black, glass-encrusted, massive, Fe-stained at pillow rim boundary, olivine-microphyric basalt.	ol, plag	0
69.1	Cone	15°36	174°49	2220	206	Black, thickly glass-encrusted, poorly vesicular, olivine-microphyric basalt. Minor Fe staining on glass interior surface.	ol, plag	1
69.2	Cone	15°36	174°49	2220	206	Glass chips of above.	plag	5

[a]Determined by digital reconstruction of the slab geometry; see section 2.4 and Appendix A.
[b]Determined by Scanning Electron Microscope (SEM). Ol, olivine; cpx, clinopyroxene; opx, orthopyroxene; plag, plagioclase; cr-sp, chrome spinel.
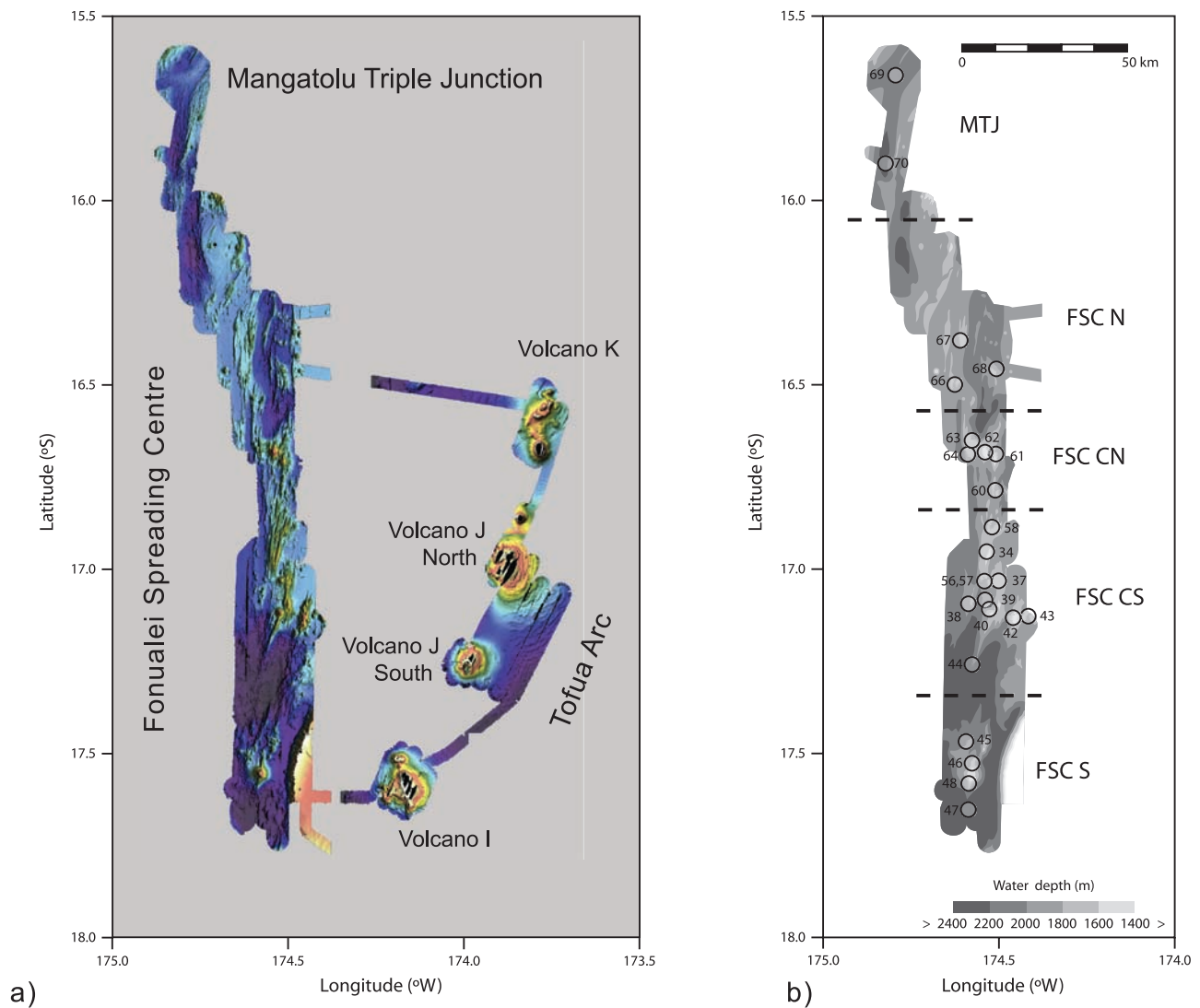
6 of 28

Figure 3. (a) Swath map of the Fonualei Spreading Center, Mangatolu Triple Junction, and adjacent volcanoes I, J, and K, produced during cruise NoToVE SS11/04. No color scale is given as it is a composite image, with different scales for different edifices. Black areas on top of volcanoes I and J were too shallow to swath map (typically < 30 m). (b) Map of the Fonualei Spreading Center with dredge locations and subdivisions used in this article: FSC S, Fonualei Spreading Center South, FSC CS, Fonualei Spreading Center Central South, FSC CN, Fonualei Spreading Center Central North, FSC N, Fonualei Spreading Center North, MTJ, Mangatolu Triple Junction. Circles and adjacent numbers indicate dredge locations and identification numbers. The water depth within the FSC is given at the bottom.

includes the adjacent submarine portion of the Tofua Arc (Volcanoes I, J, and K). These volcanoes currently appear to be inactive: swath mapping and dredging of the volcanic centers I, J south, J north, and the southern portion of K show that they have flat, carbonate-capped tops and show no significant morphological evidence of recent activity; recovered dredge samples are reefal limestone (Volcano I), Fe-Mn-stained altered lavas and volcaniclastic sediments (Volcano J) and altered lavas, Mn-coated and live deep sea corals (Volcano K) [*Arculus*, 2004]. This contrasts with all the other submarine edifices from the northern Tofua arc, between Tongatapu and Tafahi (see Figure 1) which display youthful volcanic morphology, sparse sediment cover,

variable hydrothermal activity, and from which fresh glassy samples were recovered [*Arculus*, 2004].

[13] Water depths in the FSC range from about 3000 m in the deepest areas to about 1000 m for the shallowest summit edifice. Particularly striking is the morphology at the southern tip of the FSC where a subvertical escarpment separates the arc from the back arc, with an elevation difference of about 2000 m. The samples presented in this study were dredged at water depths ranging from 1240 m to 2620 m. Figure 3b shows a simplified version of the map with dredge locations. In order to investigate geochemical changes along the length of the FSC, we subdivided the 250 km long spreading center into five parts: Fonualei Spreading Center South (FSC S), Fonualei Spreading

Center Central South (FSC CS), Fonualei Spreading Center Central North (FSC CN), and Fonualei Spreading Center North (FSC N), as well as the Mangatolu Triple Junction (MTJ). This subdivision is mainly based on the grouping of dredge stations around definite ridge structures such as cones and ridge summits (Figure 3a). A summary of the dredge stations and description of the dredge hauls can be found in Table 1.

3.2. Sample Preparation

[14] Most of the samples recovered from the FSC are fragments of pillow basalts and lava flows, comprising vesicular, relatively phyric cores and dense, black glassy rims of variable thickness, but usually ranging from <1 mm to a few centimeters. The glassy rims were chiseled off, mounted in epoxy disks, and polished for analysis. Typically, the glassy rims contain some phenocrysts; a few samples contained too many phenocrysts for suitable analysis and were rejected from the sample set (e.g., ND59, ND41, and ND44). Most dredge hauls returned single lithologies. In the few cases where more than one lithology were returned, one sample of each was mounted and analyzed. A freshly erupted glassy sample from Tofua Volcano, situated on the arc front (see Figure 1) was collected in October 2004; analytical data for this sample are presented as a reference with respect to the back-arc samples.

3.3. Analysis
3.3.1. Major Elements

[15] The major elements (Na, Mg, Al, Si, Ca, K, Fe, Ti) of the glasses were determined with energy-dispersive spectrometry using a JEOL 6400 Scanning Electron Microscope (SEM) at the Electron Microscopy Unit (EMU), Research School of Biological Sciences, Australian National University (ANU). The probe current used was 1 nA, scanning an area $50-100$ μm wide, or smaller in the presence of numerous small phenocrysts; the wide scan area results in negligible volatile loss in the hydrous glasses. Five to ten spots were analyzed on each sample, and an average and standard deviation calculated. The relative standard deviations are always below 5% for all oxides present at levels higher than 5 wt% (MgO, Al_2O_3, SiO_2, CaO, FeO). Na_2O also typically has relative standard deviations lower than 5% but with a few exceptions at 6%. The minor oxides, K_2O and TiO_2, show a greater variability due to the closeness to the limit of detection of this instrument; TiO_2 in particular shows deviations up to 20%. More precise data for Ti were acquired with laser ablation inductively coupled plasma mass spectrometry (LA-ICP-MS; see below); cross-check with Electron Microprobe (i.e., EPMA) WDS analysis show that all three techniques (SEM, LA-ICP-MS, and EPMA) yield comparable compositions (generally better than 5%). The major elements for the phenocrysts (Na, Mg, Al, Si, Ca, K, Fe, Ti, Cr) were analyzed at the EMU on the JEOL 6400 and on a Hitachi 4300 Shottky Field Emission SEM, using a similar procedure as for the glasses, but using the instrument in spot mode as opposed to area scans.

3.3.2. Volatiles (H_2O, Cl, S)

[16] Preliminary H_2O contents were determined on a subset of the sample series using Fourier Transform Infra-Red (FTIR) spectroscopy. The samples were mounted in epoxy, thinned to an approximate thickness of 200 μm and doubly polished. A detailed description of the method, as well as molar absorptivity constants, can be found in the work of *Ihinger et al.* [1994]. The EPMA and SEM totals are approximately the same for the 30 samples (see Table 3 below) and therefore the H_2O contents of all the samples are expected to be within the same range. A detailed study of the H_2O contents of all the samples is planned using Secondary Ion Mass Spectroscopy (SIMS).

[17] All glasses were analyzed for Cl and S with wavelength-dispersive spectrometry using a Cameca SX100 Electron Microprobe in the Research School of Earth Sciences (RSES) at the ANU. Cl was calibrated on scapolite and S calibrated on anhydrite. Owing to the tendency for the S $K\alpha$ X-Ray line to shift and change shape with different valence states [*Carroll and Rutherford*, 1988], we adopted a peak-integral analysis method rather than the more conventional peak-background-background technique. In the peak integral method, the spectrometer is scanned across the peak and after a background curve is fitted and those counts removed, the peak count is taken as the integral of the peak. Several repeats of the measurements allow the counting statistics to be improved. We have found this technique to be robust and effective at determining S abundances as low as $30-50$ ppm (over 10 min of analysis time required). The analysis was conducted using mixed conditions; 15 kV, 10 nA, 10 μm beam size, for the major elements which were used for matrix corrections; followed by 15 kV, 100 nA, 20 μm beam size for the trace S. To gain as many counts as possible, the S line was measured using two spectrometers equipped with a PET and a LPET crystal, respectively. Throughout the sessions, Cl and S concentrations were checked at regular intervals using the reference glass standards NIST610 (470 ppm Cl) and VG2 (1350 ppm S). At least five spots were analyzed on each glass; relative standard deviations for S vary between 1% at the 1000 ppm level, 10% at the 100 ppm level down to 20% at the detection limit around $30-50$ ppm. In the case of Cl, all averages have relative standard deviation <5% and typically below 2%.

3.3.3. Trace Elements

[18] Minor and trace elements for the glasses were determined at the RSES using a Laser Ablation (LA) ICP-MS system equipped with an ArF Excimer laser operating at 193 μm wavelength. Spot sizes were 83 μm for most elements, and 112 μm for the low-abundance elements (such as Re). The laser pulse rate was 8 Hz. A NIST612 glass was used as a primary standard, and results were checked for accuracy using a BCR-2G glass as a secondary standard. The primary standard was measured twice every $8-10$ sample analysis, and all primary standard analyses were plotted in order to discard anomalous points, as it is known that NIST glasses are heterogeneous in certain elements [*Eggins and Shelley*, 2002]. Four points on each sample were analyzed and averaged. CaO values obtained from SEM analyses were used as internal standards. We chose CaO over SiO_2 as an internal standard as the BCR-2G concentrations obtained were closer to the references values when using CaO. The values for NIST612 are a compilation of preferred values taken from the original NIST certificate [*Reed*, 1992], from *Pearce et al.* [1997] as well as from

Table 2. Representative Analyses of Phenocrysts From the Fonualei Spreading Center[a]

Sample ID Mineral	61.2 OL (Fo89)	69.1 OL (Fo83)	45.1 PLAG (An88)	67.3 PLAG (An74)	61.1 CPX	40.1 CPX	61.1 OPX	40.1 OPX	38.1 Cr-SP	61.2 Cr-SP
SiO_2	40.88	40.34	46.00	51.07	53.40	52.45	55.52	55.55	0.26	0.22
TiO_2	<0.20	<0.20	<0.20	<0.20	<0.24	0.28	<0.24	<0.24	0.32	0.29
Al_2O_3	<0.18	<0.22	33.47	30.23	2.38	3.64	1.84	0.74	13.20	12.07
Cr_2O_3	<0.20	<0.24	<0.20	<0.24	0.79	0.32	0.46	<0.24	52.09	50.89
FeO_{tot}	10.76	15.79	0.91	0.97	5.95	7.91	9.00	10.97	21.82	23.94
MgO	48.33	43.96	0.37	0.49	19.35	18.79	30.62	28.76	12.13	10.59
CaO	0.27	0.35	17.83	14.58	18.23	17.07	2.49	3.29	0.14	0.33
Na_2O	<0.16	<0.18	1.29	2.87	<0.16	0.15	<0.16	0.14	<0.16	<0.18
K_2O	<0.10	<0.12	<0.10	<0.10	<0.12	<0.12	<0.10	<0.10	<0.10	<0.12
Total	100.24	100.44	99.87	100.21	100.10	100.61	99.93	99.45	99.96	98.33

[a]OL, olivine; Fo, forsterite content; PLAG, plagioclase; An, anorthite content; CPX, clinopyroxene; OPX, orthopyroxene; Cr-SP, chrome spinel.

S. M. Eggins (personal communication, 2006). The BCR-2G values are from the GeoReM preferred values compilation by K. P. Jochum and F. Nehring (available online at http://georem.mpch-mainz.gwdg.de/) All NIST612 and BCR-2G references values, as well as the BCR-2G values obtained during analysis of the sample set, are shown at the bottom of Table 4.

4. Results

4.1. Petrography and Mineralogy

[19] The Fonualei Spreading Center glasses are aphyric to porphyric basalts and basaltic andesites. Their vesicularity was determined visually and varies between 0 and approximately 40% and correlates approximately with water depth, with lower vesicularity found in the samples erupted at greater depth. This is expected as greater water pressure alleviates syneruptive degassing.

[20] Optical and SEM investigation of the samples revealed the presence of phenocrysts in most samples. The main phases are olivine, pyroxene, plagioclase, and chrome spinel, consistent to a first approximation with cotectic crystallization of these phases. No Fe-Ti oxides were found in any of the samples. Compositions of representative mineral phases are summarized in Table 2.

[21] Olivine phenocrysts with cores of Fo_{89} to Fo_{83} are present in about 50% of the samples. Some of the bigger crystals (100 μm) sometimes show zoning, ranging typically over 2 or 3 Fo units between core (higher Fo) and rim (lower Fo). Pyroxene phenocrysts are present in about 75% of the samples. They are mostly clinopyroxene (augite - cpx) and orhopyroxene (opx); a few samples also contain pigeonite. Opx and cpx are often found in the same crystal, in either opx core – cpx rim zones or in diffuse patches. Some show clear boundaries, which may represent exsolution lamellae. Their Cr_2O_3 contents range from below detection on the SEM (<0.3 wt%) to 1.3 wt%. The Al_2O_3 is typically below 2% in the opx and between 2 and 5% in the cpx. Plagioclase crystals are present in about 65% of the samples. They have anorthite contents between 70 and 90 mol%. Thirty percent of the samples contain chrome spinel, with Cr number (Cr#) ranging from 64 to 76 (Cr# = $(X_{Cr}/(X_{Al} + X_{Cr}))$ * 100).

[22] Generally, the volumetric ratio of glass to phenocrysts is high enough to ensure that the composition of the glass is a suitable approximation for the composition of the parental melt.

4.2. Glasses: Major Oxides

[23] Major oxide abundances are listed in Table 3. The FSC samples range from 49 to 55 wt% SiO_2, and the Tofua sample contains 56 wt% SiO_2. In order to display the data in conventional major element variation diagrams, all compositions were recalculated to 100%, volatile free. The glass compositions are shown in Figure 4 in a "Total Alkali versus Silica" plot (TAS). The lavas from the FSC are relatively primitive, consisting of mostly basaltic andesite. The three northernmost samples (70.1, 69.1, and 69.2) are basalt; they were dredged from the center (69.1, 69.2) and just south (70.1) of the Mangatolu Triple Junction (MTJ). These three samples show geochemical characteristics which are systematically different from the rest of the FSC, in the major element geochemistry where they tend to have lower SiO_2 contents and higher $Na_2O + K_2O$, as well as in their trace element systematics as will be discussed below. Therefore we differentiate between theses two groups and refer to the samples from the triple junction as MTJ and to the others from further south as FSC. Figure 4 also displays data from previous studies of the Lau Basin. In contrast to the relatively undifferentiated FSC, the samples dredged from the VFR show a complete differentiation suite from basalt to rhyolite, consistent with findings by *Fretzdorff et al.* [2006] and the fact that rifting is usually associated with more felsic lavas. For a given SiO_2, the FSC samples have generally lower $Na_2O + K_2O$ compared to the CLSC and the VFR. The Tofua sample has an andesitic composition, also showing lower alkali contents than back-arc samples with similar SiO_2 contents.

[24] All samples contain between 4.2 and 8.2 wt% MgO with Mg numbers (Mg# = $(X_{Mg}/(X_{Mg} + X_{Fe}))$ * 100, with all Fe as Fe^{2+}) between 42 and 65 (Table 3). Figure 5 shows MgO variation diagrams for major and minor elements. Liquid lines of descent can be observed, with MgO positively correlated with CaO, and negatively with FeO, K_2O and TiO_2. There is no inflexion in the trend for TiO_2, which rules out Fe-Ti-oxide saturation, consistent with the petrographic observations. The MTJ samples have higher Na_2O, TiO_2 and Al_2O_3 as well as lower SiO_2 for a given MgO than the FSC samples do, giving the MTJ a more MORB-like affinity than the FSC.

4.3. Volatiles

[25] Volatile contents are given in Table 3. The water contents are around $1-1.6$ wt%, which is in the middle of

Table 3. Major and Volatile Element Analyses of Tofua Volcano and the Fonualei Spreading Center

Sample ID	SEM (wt%)									Mg#[a]	FTIR (wt%) H$_2$O	EPMA (ppm)	
	SiO$_2$	TiO$_2$	Al$_2$O$_3$	FeO$_{tot}$	MgO	CaO	Na$_2$O	K$_2$O	Total			S	Cl
Tofua													
TO2.4	56.73	0.83	12.68	11.73	4.17	8.98	1.99	0.64	97.74	39		30	318
FSC S													
47.1	53.22	0.64	15.77	7.87	6.44	11.57	1.84	0.57	97.92	59	1.52	120	791
48.1	54.06	0.72	14.69	9.98	5.35	10.14	1.64	0.60	97.16	49	1.01	40	989
46.1	53.17	0.68	14.55	9.83	6.39	10.82	1.78	0.41	97.62	54	1.18	67	733
45.1	53.00	0.65	14.88	8.91	6.44	11.21	1.73	0.50	97.32	56		74	879
FSC CS													
42.1	52.99	0.57	15.70	7.35	7.39	12.04	1.75	0.59	98.38	64	1.11	39	756
43.1	50.51	0.48	15.47	8.35	7.78	13.32	1.40	0.52	97.84	62	1.18	115	556
40.1	52.71	0.42	15.25	9.28	6.85	11.50	1.37	0.35	97.74	57	1.37	54	821
38.1	53.25	0.49	14.43	7.64	7.53	12.14	1.57	0.47	97.52	64	1.38	121	598
39.1	52.53	0.49	14.49	9.97	6.44	10.97	1.40	0.38	96.67	54	1.60	89	830
37.1	51.33	0.59	15.42	8.69	6.98	12.30	1.82	0.37	97.49	59	1.12	145	1025
37.2	51.25	0.52	15.91	8.30	6.95	12.69	1.78	0.35	97.74	60	1.29	138	977
56.1	54.00	0.40	14.62	8.38	7.26	11.87	1.45	0.32	98.04	61	1.16	42	646
57.1	54.22	0.39	14.34	8.36	7.32	11.77	1.38	0.30	98.09	61	1.04	46	653
34.1	55.90	0.43	15.20	8.99	4.92	10.12	1.61	0.51	97.68	49	1.18	43	915
58.2	54.18	0.61	15.00	10.52	4.21	9.31	1.68	0.53	96.02	42		72	841
FSC CN													
60.1	53.89	0.41	15.08	8.31	6.21	10.84	1.50	0.51	96.74	57		47	808
60.2	53.54	0.40	15.04	8.09	6.59	11.26	1.30	0.46	96.67	59		60	937
61.1	54.88	0.37	14.50	8.05	6.54	11.04	1.43	0.48	97.29	59		28	826
61.2	54.79	0.44	13.95	8.03	6.80	11.19	1.41	0.43	97.04	60		33	816
62.1	54.27	0.41	14.26	8.35	6.85	11.30	1.34	0.47	97.24	59		31	1063
64.1	54.34	0.55	13.63	8.52	7.59	10.11	1.64	0.58	96.97	61		99	924
63.1	53.69	0.61	14.74	8.94	6.05	10.56	1.66	0.48	96.73	55		71	1068
63.2	53.40	0.57	14.92	8.88	6.24	10.72	1.63	0.48	96.84	56		74	1031
FSC N													
66.1	52.57	0.44	14.88	7.56	7.43	12.19	1.45	0.42	96.94	64		159	561
68.1	53.27	0.50	14.03	7.92	8.23	11.83	1.55	0.56	97.89	65		76	681
67.3	52.31	0.61	15.03	9.24	6.90	11.30	1.84	0.48	97.70	57		91	979
MTJ													
70.1	49.23	0.78	16.10	7.87	8.21	12.78	1.94	0.15	97.06	65		889	219
69.1	49.73	1.10	15.48	8.95	6.75	11.41	2.64	0.32	96.38	57		922	447
69.2	50.13	0.95	15.76	8.57	7.04	11.71	2.44	0.35	96.93	59		774	483

[a]Mg# = (XMg/(XFe + XMg)) × 100, Fe as Fe^{2+}, X, mole fraction.

the typical range for backarc basins (0.2–2.5 wt% H$_2$O [*Langmuir et al.*, 2006]).

[26] Sulfur and chlorine are strongly decoupled, and show markedly different behavior in the MTJ and in the FSC (Figure 6). S contents range from close to the limit of detection (∼30 ppm) to 160 ppm in the FSC, whereas the MTJ values are higher at 770–920 ppm; the latter correspond approximately to MORB values [*Sakai et al.*, 1984]. Within the FSC, S contents decrease with increasing SiO$_2$, which is unusual as S is considered to behave like a moderately incompatible element in partial mantle melting [*McDonough and Sun*, 1995], yet consistent with observations from the rest of the Lau Basin [*Nilsson Farley*, 1994]. Cl contents range from 560 to 1060 ppm in the FSC samples (10–50 times the MORB value (20–50 ppm) [*Michael and Schilling*, 1989]) and are lower in the MTJ, with contents between 220 and 480 ppm. Cl contents show a broad inverse correlation with Mg#, as expected from the incompatible behavior of Cl during crystallization of basaltic melts [*Kent et al.*, 2002].

4.4. Trace Elements

[27] Trace element abundances are presented in Table 4. N-MORB normalized trace element patterns are presented in Figure 7a, arranged in a standard sequence (from left to right) of increasing compatibility in residual peridotite minerals during partial melting of the upper mantle. In Figure 7b, we divided the N-MORB-normalized data by Yb, a slightly incompatible yet conservative element in subduction environments. This relocates the geochemical patterns to Yb = 1 and minimizes effects due to partial melting, fractionation, and accumulation of phenocrysts [*Pearce et al.*, 2005] and facilitates the comparison of the various patterns; we use the same approach in subsequent spidergrams. All samples have patterns very different to N-MORB, consistent with BABB and IAB geochemistry (e.g., summary in the work of *Pearce and Stern* [2006]). The main features are strong LILE (Cs, Ba, Rb, Th, U, K, Sr), Pb and small P enrichments, and HFSE depletion (Nb, Ta, Zr, Hf) relative to N-MORB. The MTJ samples have
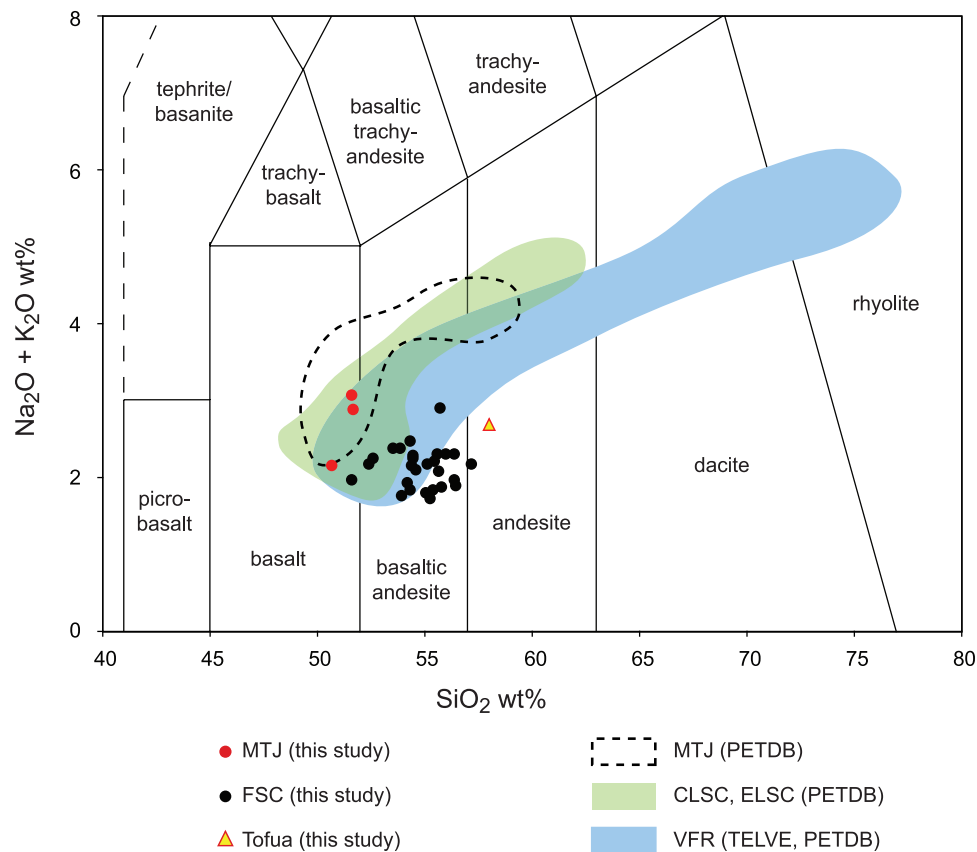
Figure 4. Total alkali versus silica (TAS) for the samples analyzed in this study (MTJ, FSC) and from other locations in the Lau Basin: MTJ, ELSC, CLSC, and VFR data from a compilation by *Langmuir et al.* [2006], available on PetDB (http://www.petdb.org [*Lehnert et al.*, 2000]); additional VFR data from R. J. Arculus (unpublished data set, 2007) for samples recovered during TELVE Cruise [*Arculus et al.*, 2003]. Compositions recalculated to 100% anhydrous. Field boundaries from *Le Maitre et al.* [1989].

less pronounced anomalies than the FSC samples; in particular, their Nb and Ta abundances are almost identical to N-MORB abundances. A decrease in intensity of the Nb and Ta anomaly from Tofua Volcano in the south to the MTJ in the north can be seen, with a steady transition within the FSC. By contrast, the intensities of LILE, Pb and P enrichments within the FSC do not change systematically from south to north. There is no systematic change in the chondrite-normalized Rare Earth Elements (REE) patterns within the FSC (Figure 8). They are essentially flat, showing about 10 times chondritic abundances, with very slight light REE (LREE) depletions or enrichments relative to the heavy REE (HREE). The MTJ samples have slightly higher REE abundances than the FSC, with small LREE depletions relative to the HREE.

4.5. Geographical Variations: Using Geochemical Maps

[28] Differences in geochemical patterns can be attributed to variable initial mantle wedge compositions and depletion history, as well as different element concentration and fractionation inherent to the subduction input (whether a melt or an aqueous phase). In order to study the various origins of the geochemical patterns, we use a set of key trace element ratios and show them in a spatial context, using a similar approach as *Pearce et al.* [2005] who

presented geochemical maps of the Marianas arc-back-arc system. The chosen element ratios are Nb/Yb (enrichment/depletion of the mantle source; the higher the value, the more fertile the mantle), Ba/Yb and Ba/La (shallow subduction tracers; the higher the value, the larger the shallow subduction component), and Nb/Ta (ultradeep subduction proxy, due to Nb retention in rutile; the larger the value, the larger the ultradeep subduction input).

[29] Figure 9 shows the geochemical maps for the FSC and the MTJ; a colored dot corresponding to the Tofua sample is shown for comparison at the bottom of each map (not in its correct geographical location). The Nb/Yb map (Figure 9a) shows an enhancement in mantle fertility from south to north, consistent with the observation of the Nb-Ta anomaly in Figure 7. This gradient can even be resolved within the FSC (Dregdes 47 to 67). The subduction proxies Ba/Yb (Figure 9b) and Ba/La (Figure 9c) show distinct differences between FSC, Tofua, and MTJ. However, within the FSC no clear trend can be seen, indicating that the subduction component does not vary systematically in this section. No systematic change in the ultra deep subduction signature (Nb/Ta, Figure 9d) variation can be seen with this mapping method, suggesting that no significant fractionation of Nb and Ta occurs over the range of depth of the generation of the subduction component. Unlike other studies [e.g., *Kent et al.*, 2002; *Pearce et al.*, 2005], we

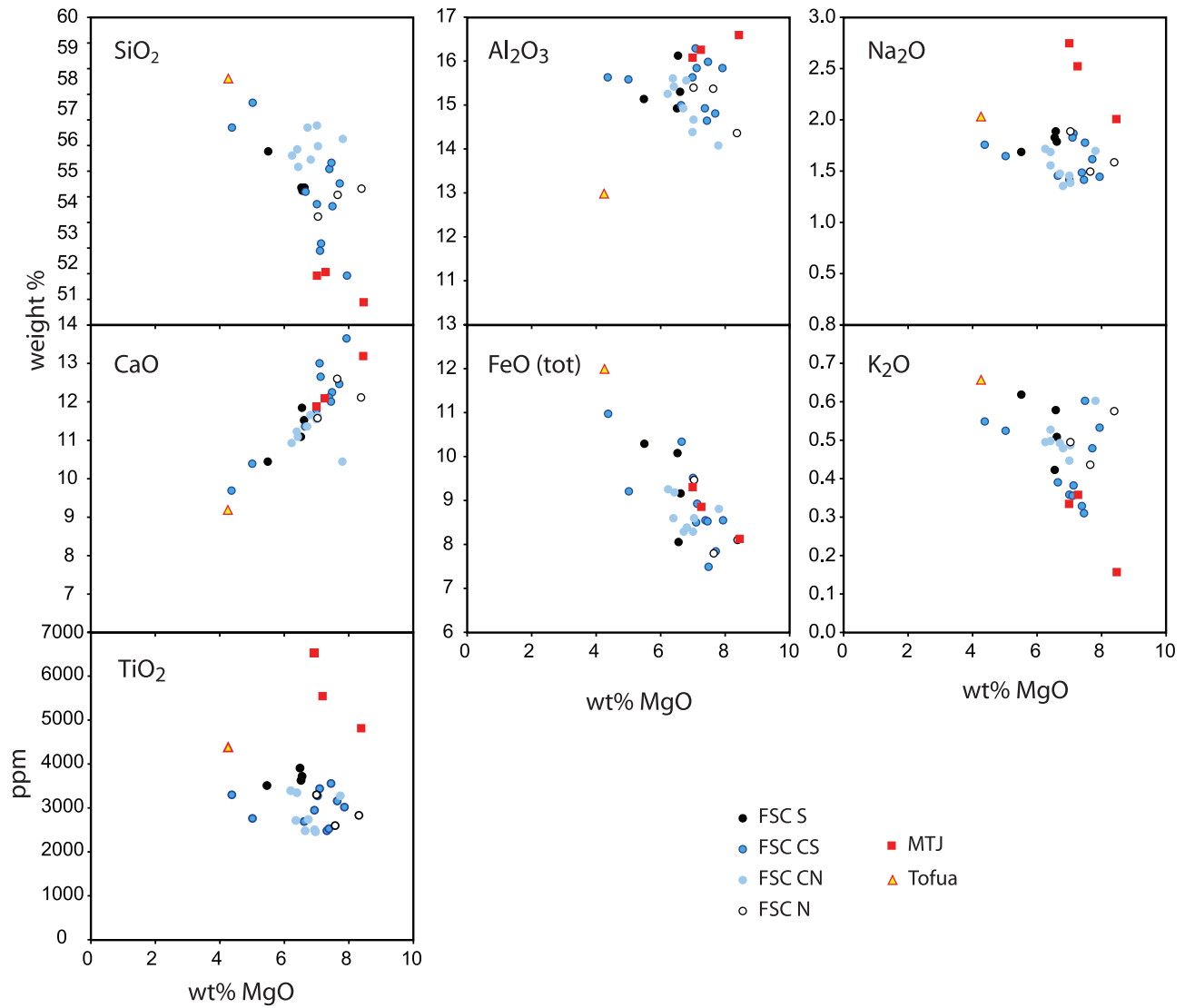**Figure 5.** Oxide-MgO variation diagrams for the FSC, MTJ, and Tofua samples. Compositions recalculated to 100% anhydrous. Abbreviations as in Figure 3b.
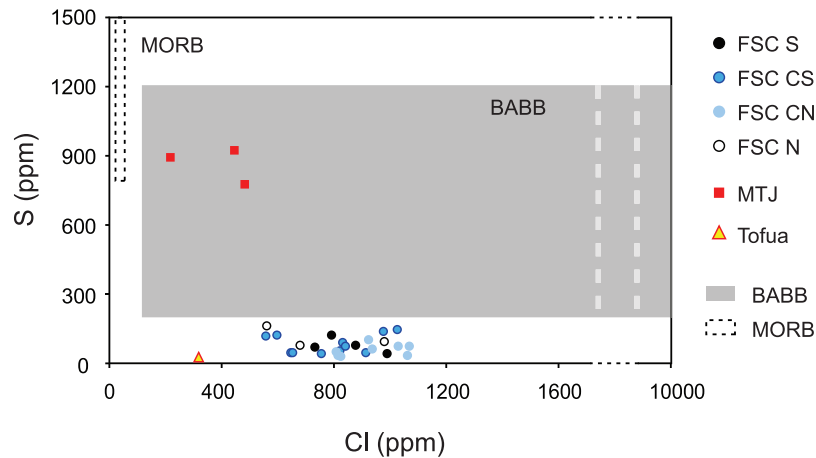

Figure 6. S versus Cl diagram for the FSC, MTJ, and Tofua samples. Abbreviations as in Figure 3b. S, Cl values for MORB and BABB from *Michael and Schilling* [1989], *Nilsson Farley* [1994], *Kent et al.* [2002], and *Wallace* [2005].

Table 4. LA-ICP-MS Analyses of Trace Elements of Tofua Volcano and the Fonualei Spreading Center

Sample ID	Li	Be	B	P	Sc	Ti	V	Cr	Co	Ni	Cu	Zn	As	Rb	Sr	Y	Zr	Nb	Mo	Cd	In	Sn
Tofua																						
TO2.4	7.2	0.26	26.1	749	45	4414	382	17	36	13	209	107	2.9	7.6	203	17.1	30	0.31	1.4	0.092	0.072	0.55
FSC S																						
47.1	4.3	0.28	7.3	706	37	3644	274	136	33	59	101	62	0.32	8.2	185	14.0	25	0.55	0.43	0.102	0.060	0.48
48.1	4.9	0.27	11.0	681	40	3529	309	11	37	33	149	78	0.74	8.8	199	13.3	22	0.54	0.53	0.102	0.065	0.47
46.1	4.5	0.26	10.2	600	40	3914	307	25	42	34	131	74	0.66	6.2	175	15.5	24	0.50	0.52	0.107	0.064	0.47
45.1	4.3	0.25	6.3	650	39	3735	294	110	33	41	111	67	0.20	7.1	221	13.4	23	0.54	0.35	0.105	0.059	0.43
FSC CS																						
42.1	4.2	0.26	7.6	812	39	3566	252	292	34	62	107	57	0.19	8.8	218	14.7	25	0.41	0.34	0.108	0.053	0.46
43.1	4.0	0.25	7.5	712	39	3041	265	141	42	65	126	62	0.18	11.1	199	12.5	17	0.34	0.29	0.097	0.053	0.37
40.1	4.2	0.20	9.9	531	39	2965	277	26	46	46	144	76	0.57	6.2	149	12.0	18	0.43	0.48	0.101	0.055	0.40
38.1	4.0	0.25	6.9	589	41	3179	261	277	35	71	109	63	0.43	7.6	161	12.8	24	0.48	0.40	0.111	0.053	0.44
39.1	3.8	0.19	9.4	465	39	2710	263	24	44	48	130	67	0.50	5.6	142	11.2	17	0.41	0.45	0.100	0.052	0.39
37.1	4.2	0.20	5.5	508	32	3446	236	23	40	47	123	65	0.17	6.5	224	13.2	22	0.36	0.30	0.110	0.053	0.46
37.2	4.5	0.20	4.5	480	35	3281	233	35	38	55	125	66	0.21	6.0	216	12.8	22	0.33	0.29	0.102	0.048	0.33
56.1	3.8	0.17	9.7	416	42	2492	256	286	37	59	112	65	0.49	5.2	139	10.2	16	0.36	0.44	0.092	0.045	0.34
57.1	3.8	0.18	9.7	448	42	2529	258	228	37	58	119	70	0.52	5.2	140	10.3	16	0.37	0.45	0.099	0.045	0.35
34.1	5.4	0.22	10.8	664	32	2778	255	31	35	30	119	84	0.71	8.2	150	12.1	19	0.54	0.57	0.106	0.052	0.39
58.2	5.1	0.23	9.3	656	37	3324	390	6.6	38	21	214	82	0.60	7.7	173	11.2	18	0.52	0.51	0.093	0.054	0.34
FSC CN																						
60.1	4.9	0.22	10.3	605	37	2714	267	84	35	59	130	68	0.61	8.3	189	10.6	18	0.57	0.47	0.090	0.047	0.27
60.2	4.9	0.25	10.5	647	38	2749	272	83	38	63	142	70	0.65	8.3	197	10.6	18	0.61	0.49	0.089	0.052	0.37
61.1	4.8	0.21	14.6	534	38	2501	264	69	33	51	120	67	0.89	8.0	183	9.6	17	0.49	0.57	0.088	0.045	0.26
61.2	4.4	0.22	10.8	553	37	2522	256	128	34	55	121	63	0.67	7.8	166	9.7	17	0.61	0.50	0.087	0.049	0.34
62.1	4.4	0.23	11.1	611	39	2474	266	120	38	64	128	66	0.75	8.3	192	9.3	17	0.66	0.52	0.080	0.049	0.36
64.1	4.9	0.31	7.2	819	36	3298	281	324	39	79	115	68	0.27	10.2	187	13.2	25	0.88	0.40	0.094	0.054	0.46
63.1	5.3	0.27	8.5	637	34	3417	263	24	39	37	134	73	0.46	8.9	147	12.7	26	1.15	0.45	0.099	0.054	0.38
63.2	5.0	0.28	8.2	664	33	3366	258	33	39	41	139	73	0.48	8.6	151	12.6	26	1.20	0.47	0.093	0.056	0.46
FSC N																						
66.1	3.8	0.20	8.3	455	38	2608	244	184	36	75	115	61	0.60	6.9	139	9.7	17	0.87	0.37	0.102	0.048	0.34
68.1	3.9	0.27	9.3	672	40	2833	245	376	38	81	118	65	0.43	10.4	198	10.1	20	0.73	0.44	0.087	0.048	0.39
67.3	4.0	0.26	5.8	611	36	3314	253	52	40	47	126	63	0.23	6.9	186	12.1	24	1.14	0.36	0.099	0.051	0.43
MTJ																						
70.1	4.3	0.32	5.3	512	36	4830	205	335	44	105	85	62	0.15	4.1	123	17.7	44	1.21	0.36	0.102	0.060	0.62
69.1	5.8	0.55	6.5	842	36	6543	244	222	41	68	65	74	0.20	8.7	141	23.3	64	2.10	0.53	0.113	0.073	0.83
69.2	5.1	0.52	5.7	831	35	5570	228	233	39	69	74	67	0.17	10.9	144	20.0	53	1.87	0.47	0.109	0.061	0.64
Primary and Secondary Standards																						
NIST612 ref	41[a]	38[a]	32[b]	55.2[c]	39[a]	41[a]	38[a]	38[a]	35.5[b]	39[b]	38[b]	38[c]	37[a]	31.7[a]	78.4[b]	38.2[a]	38[a]	38[a]	38[a]	28[a]	38[a]	38[c]
BCR-2G ref[d]	9	2.3	6	1589	33	14100	425	17	38	13	21	125	0.65[f]	47	342	35	184	12.5	270	0.2	0.11	2.6
BCR-2G NK[e]	9.3	2.2	6.9	2112	31.6	13879	398	15.8	39.1	12.2	18.8	139	0.92	47.4	332	31.8	175	12.2	264	0.19	0.10	2.2

Table 4. (continued)

Sample ID	Sb	Cs	Ba	La	Ce	Pr	Nd	Sm	Eu	Gd	Dy	Er	Tm	Yb	Lu	Hf	Ta	W	Re	Tl	Pb	Bi	Th	U
Tofua																								
TO2.4	0.065	0.44	175	2.1	5.4	0.99	5.0	1.9	0.69	2.7	3.2	2.2	0.30	2.2	0.32	1.1	0.021	0.083	bdl	0.057	2.99	0.023	0.22	0.183
FSC S																								
47.1	0.013	0.20	81	2.6	6.3	1.01	4.8	1.7	0.63	2.2	2.5	1.7	0.23	1.7	0.26	0.83	0.036	0.031	0.0015	0.091	1.35	0.025	0.26	0.150
48.1	0.023	0.27	84	2.5	6.1	1.08	4.7	1.7	0.62	2.2	2.4	1.6	0.21	1.6	0.24	0.76	0.032	0.038	0.0013	0.104	1.56	0.032	0.26	0.166
46.1	0.019	0.18	62	2.2	5.7	0.96	4.7	1.7	0.65	2.3	2.8	1.9	0.26	1.9	0.29	0.80	0.033	0.032	0.0016	0.067	1.18	0.024	0.20	0.115
45.1	bdl	0.14	57	2.6	6.5	1.04	4.9	1.6	0.62	2.1	2.4	1.6	0.21	1.6	0.25	0.74	0.037	0.025	0.0015	0.077	1.12	0.025	0.20	0.115
FSC CS																								
42.1	bdl	0.18	66	2.4	6.1	0.97	5.0	1.8	0.67	2.4	2.7	1.7	0.24	1.7	0.26	0.82	0.030	0.031	bdl	0.108	1.67	0.027	0.22	0.151
43.1	bdl	0.20	35	2.9	7.3	1.16	5.6	1.7	0.59	2.0	2.2	1.5	0.21	1.5	0.23	0.56	0.021	0.032	0.0017	0.111	1.19	0.031	0.26	0.150
40.1	0.019	0.16	50	1.9	4.7	0.76	3.7	1.3	0.50	1.8	2.2	1.5	0.19	1.5	0.23	0.63	0.028	0.033	0.0017	0.064	1.04	0.025	0.19	0.109
38.1	0.013	0.16	68	2.6	6.4	0.97	4.9	1.7	0.60	2.1	2.4	1.6	0.21	1.6	0.24	0.78	0.029	0.034	0.0018	0.079	1.58	0.028	0.26	0.152
39.1	0.015	0.15	45	1.7	4.4	0.71	3.4	1.2	0.45	1.7	2.0	1.4	0.19	1.4	0.22	0.57	0.026	0.032	0.0017	0.065	1.04	0.024	0.17	0.101
37.1	bdl	0.11	40	2.2	6.0	1.02	4.9	1.7	0.63	2.1	2.5	1.6	0.21	1.6	0.24	0.74	0.022	0.023	bdl	0.058	0.96	0.027	0.18	0.090
37.2	bdl	0.10	39	2.1	5.6	0.90	4.6	1.5	0.59	2.0	2.4	1.6	0.21	1.6	0.23	0.73	0.022	0.025	0.0078	0.064	0.89	0.029	0.17	0.081
56.1	0.015	0.14	54	1.5	3.9	0.62	3.1	1.1	0.43	1.5	1.8	1.2	0.17	1.3	0.19	0.54	0.025	0.028	n/a	0.050	1.01	0.021	0.15	0.084
57.1	0.016	0.15	54	1.6	3.9	0.62	3.1	1.1	0.43	1.5	1.8	1.3	0.17	1.3	0.20	0.54	0.026	0.032	0.0028	0.060	1.06	0.019	0.15	0.080
34.1	0.017	0.21	76	2.2	5.3	0.81	4.0	1.4	0.49	1.8	2.1	1.5	0.20	1.6	0.25	0.64	0.038	0.043	0.0017	0.080	1.30	0.025	0.23	0.136
58.2	bdl	0.21	86	2.1	5.0	0.80	4.1	1.4	0.52	1.8	2.1	1.5	0.18	1.5	0.23	0.61	0.033	0.039	0.0020	0.075	1.31	0.026	0.22	0.145
FSC CN																								
60.1	bdl	0.20	68	2.3	5.6	0.86	4.2	1.4	0.50	1.7	1.9	1.3	0.19	1.4	0.21	0.61	0.039	0.037	n/a	0.089	1.30	0.029	0.24	0.137
60.2	0.013	0.21	72	2.3	5.6	0.90	4.4	1.4	0.51	1.8	2.0	1.4	0.18	1.4	0.21	0.62	0.039	0.038	0.0014	0.077	1.27	0.025	0.25	0.141
61.1	0.012	0.21	73	2.1	5.2	0.78	3.8	1.3	0.46	1.5	1.8	1.2	0.17	1.2	0.19	0.57	0.033	0.046	n/a	0.083	1.36	0.028	0.23	0.132
61.2	0.017	0.20	68	2.1	5.1	0.81	3.9	1.3	0.46	1.6	1.9	1.2	0.17	1.3	0.19	0.59	0.040	0.039	0.0012	0.064	1.16	0.021	0.24	0.132
62.1	0.019	0.21	75	2.6	6.0	0.92	4.4	1.4	0.47	1.6	1.8	1.2	0.16	1.3	0.19	0.58	0.046	0.044	n/a	0.075	1.23	0.024	0.29	0.140
64.1	bdl	0.21	94	3.0	7.1	1.13	5.5	1.9	0.63	2.3	2.5	1.7	0.22	1.7	0.26	0.83	0.058	0.047	0.0010	0.102	1.61	0.028	0.33	0.205
63.1	bdl	0.18	77	2.9	7.0	1.04	5.0	1.6	0.58	2.0	2.3	1.6	0.22	1.6	0.25	0.80	0.081	0.043	0.0025	0.082	1.21	0.028	0.36	0.149
63.2	0.012	0.19	80	2.9	6.8	1.05	5.1	1.7	0.58	2.1	2.4	1.6	0.22	1.7	0.25	0.83	0.076	0.044	0.0018	0.073	1.10	0.022	0.37	0.146
FSC N																								
66.1	0.014	0.13	67	2.1	5.0	0.78	3.9	1.3	0.46	1.6	1.8	1.3	0.17	1.3	0.19	0.58	0.057	0.039	0.0014	0.064	1.04	0.021	0.23	0.114
68.1	bdl	0.21	77	2.7	6.5	1.06	5.2	1.6	0.56	1.9	2.0	1.3	0.17	1.3	0.19	0.66	0.048	0.041	bdl	0.083	1.11	0.024	0.29	0.171
67.3	bdl	0.14	71	2.7	6.4	1.01	4.9	1.6	0.59	2.1	2.3	1.5	0.21	1.5	0.23	0.78	0.073	0.038	0.0015	0.064	1.05	0.021	0.31	0.136
MTJ																								
70.1	bld	0.09	23	2.1	6.0	1.02	5.4	2.1	0.80	2.9	3.5	2.2	0.29	2.2	0.31	1.3	0.079	0.028	0.0013	0.030	0.51	0.012	0.18	0.067
69.1	bdl	0.28	37	3.5	9.7	1.58	8.1	2.9	1.06	3.9	4.6	2.9	0.39	2.9	0.41	1.8	0.140	0.051	0.0011	0.077	0.75	0.013	0.34	0.167
69.2	bdl	0.34	41	3.3	9.1	1.40	7.0	2.5	0.92	3.2	3.8	2.4	0.32	2.4	0.34	1.4	0.116	0.055	n/a	0.113	0.72	0.014	0.36	0.195
Primary and Secondary Standards																								
NIST612 ref	38[a]	41[a]	38.5[a]	35.7[a]	38.6[a]	37[a]	35.7[a]	37.5[a]	35.4[a]	38[a]	36[c]	38.5[a]	37[a]	39[a]	36.7[a]	37[a]	41[a]	40[c]	8[a]	15.5[a]	38.6[b]	33[a]	37.8[a]	37.4[a]
BCR-2G ref[d]	0.35	1.16	683	24.7	53.3	6.7	28.9	6.59	1.97	6.71	6.44	3.7	0.51	3.39	0.5	4.84	0.78	0.5	0.006	0.3	11	0.05	5.9	1.69
BCR-2G NK[e]	0.29	1.18	675	24.4	52.2	6.4	25.9	6.6	1.95	6.8	6.3	3.6	0.48	3.4	0.49	4.6	0.76	0.50	0.010	0.28	10.50	0.050	5.90	1.66

aPreferred values taken from S. M. Eggins (personal communication, 2006).
bPreferred values taken from *Reed* [1992].
cPreferred values taken from *Pearce et al.* [1997].
dBCR-2G GeoReM preferred values (http://georem.mpch-mainz.gwdg.de/).
eBCR-2G values obtained as secondary standards during analysis of the sample set, using CaO = 7.06 wt% as internal standard (from GeoReM).
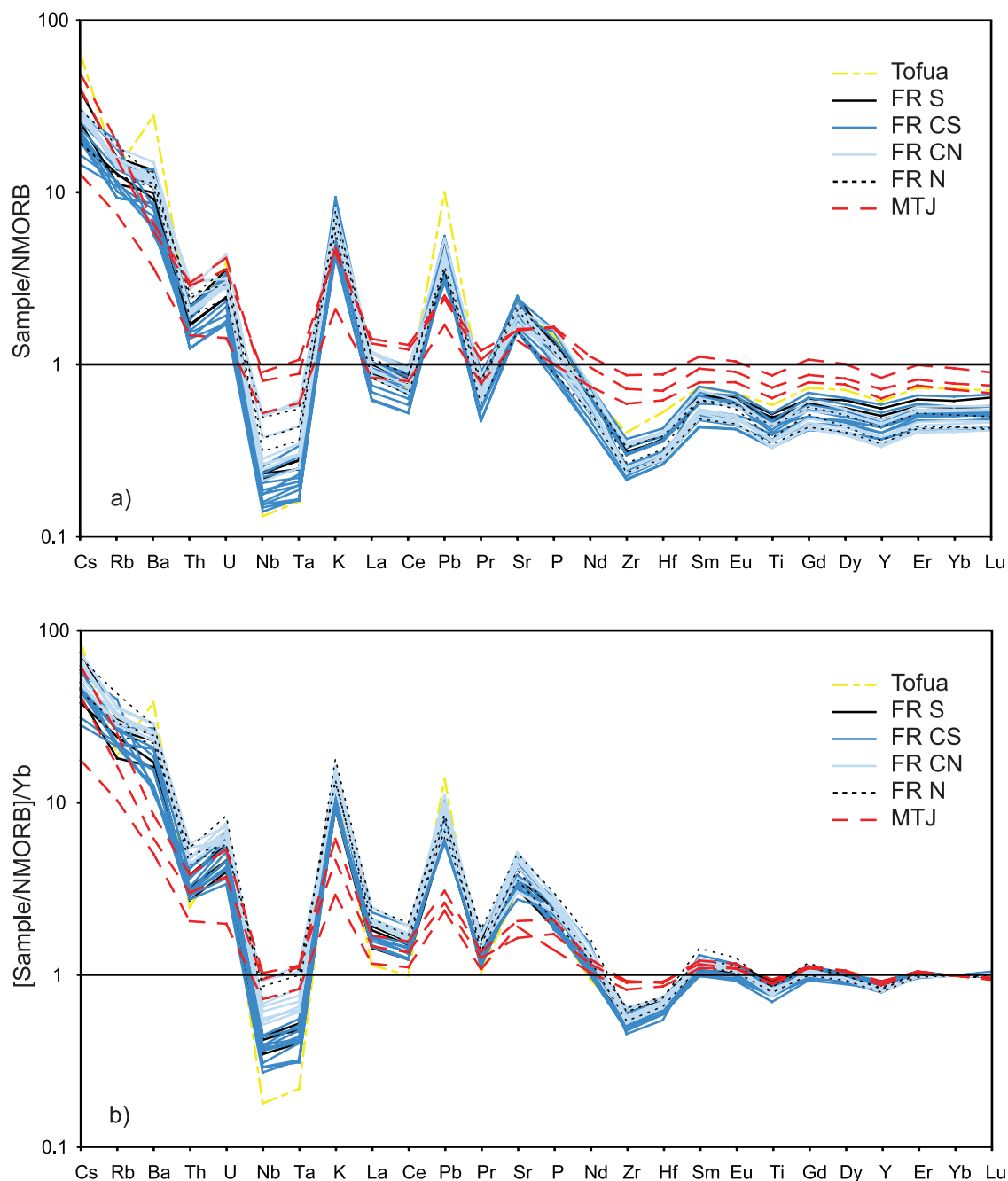fAs value from *Govindaraju* [1994].

Figure 7. (a) N-MORB normalized incompatible trace element patterns showing all FSC, MTJ, and Tofua samples. N-MORB normalization values from *Sun and McDonough* [1989], abbreviations as in Figure 3b. (b) Same sample set as Figure 7a, additionally normalized to Yb.

do not use subduction input tracers that have a HFSE in their denominator, such as Ba/Ta or Ba/Nb, since Ta and Nb change significantly with latitude in the FSC; therefore a decreasing ratio does not allow a distinction between an increase in mantle fertility and a decrease in subduction signature.

5. Discussion

[30] The Fonualei Spreading Center shows distinct trends in geochemistry, both in elemental abundances and in ratios: there are significant differences between the FSC and the

MTJ, and between the FSC and the Lau Basin. This can be see in Figure 10, which shows selected element ratios used previously for geochemical mapping (Nb/Yb, Ba/Yb, and Nb/Ta) for the samples from this study (FSC and MTJ), with fields for BABB from the Lau Basin and samples from the Tofua arc. Unlike classic BABBs, which are transitional between MORB and island arc basalts (IAB), the samples from the FSC have major and minor trace elements systematics that are similar to those of the adjacent Tofua arc. In contrast, the MTJ samples have more MORB-like affinities and are similar to Lau BABB, as was shown in
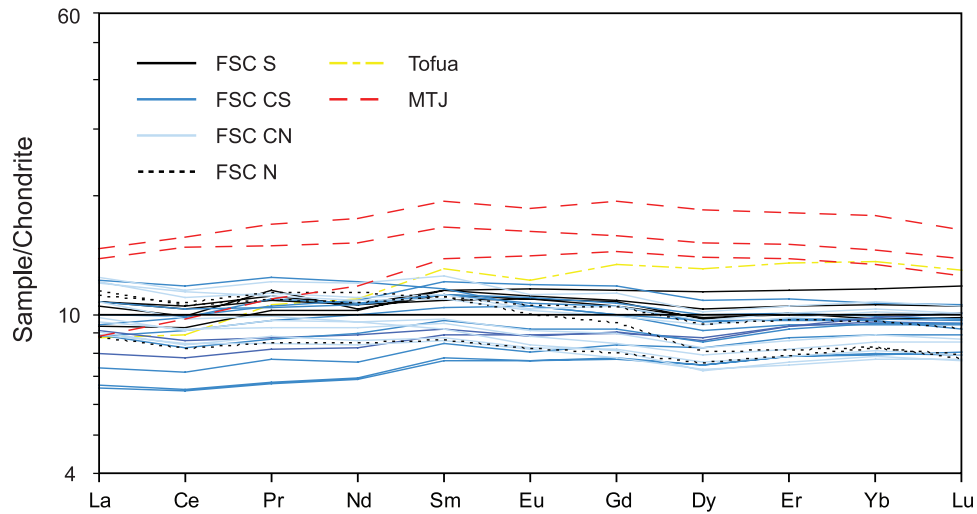
Figure 8. Chondrite-normalized rare Earth element (REE) patterns for FSC, MTJ, and Tofua samples. Abbreviations as in Figure 3b. Normalization values from *McDonough and Sun* [1995].
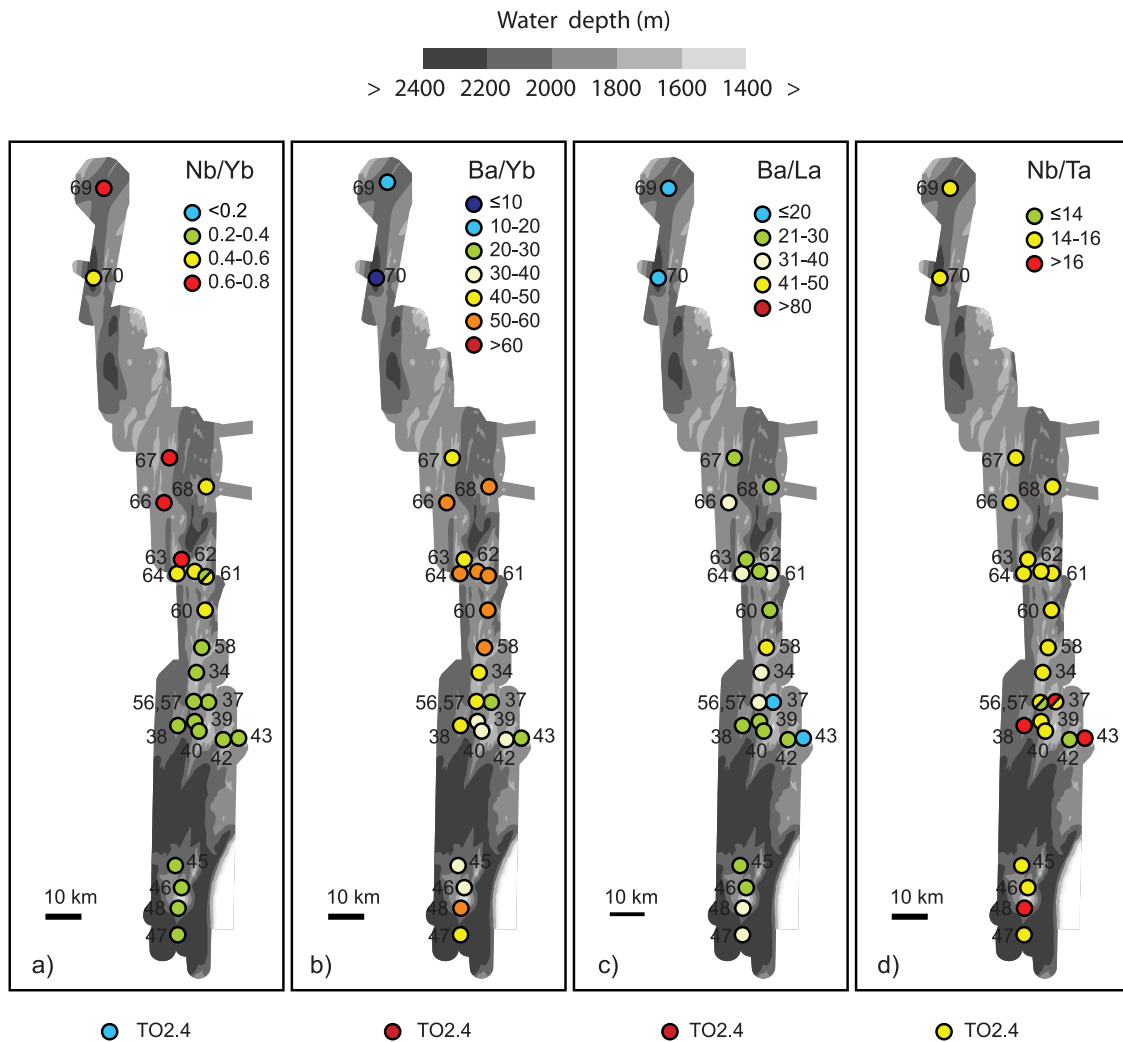
Figure 9. Geochemical maps of the Fonualei Rifts. (a) Nb/Yb (proxy for mantle fertility), (b) Ba/Yb, and (c) Ba/La (proxies for subduction component), (d) Nb/Ta (proxy for ultradeep subduction component).
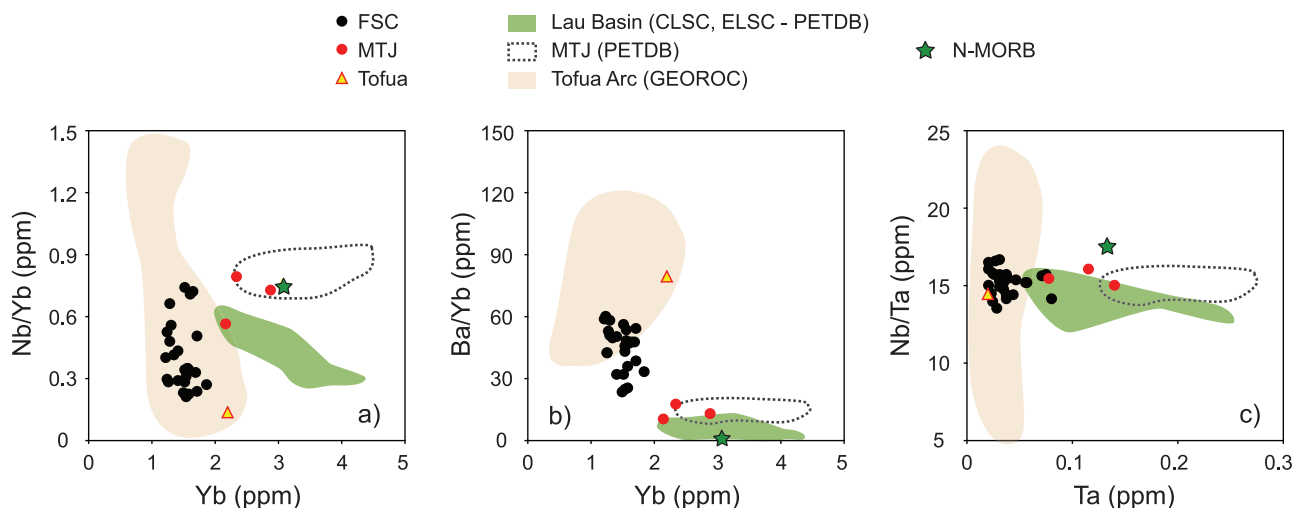
Figure 10. (a) Nb/Yb versus Yb, (b) Ba/Yb versus Yb, and (c) Nb/Ta versus Ta showing the range of trace element ratios of the FSC in comparison with BABB from the Lau Basin and with the adjacent Tofua Arc. Data from PetDB (http://www.petdb.org [*Lehnert et al.*, 2000]) and a GEOROC compilation ("TONGA ARC.csv," available at http://georoc.mpch-mainz.gwdg.de/georoc/).

previous studies [*Falloon et al.*, 1992; *Sun et al.*, 2003]. These differences reflect varying melt sources, subduction input and mantle depletion.

[31] In the following discussion we use our geochemical data to assess the melting environment of the FSC basalts, in particular by estimating the mantle porential temperature, the temperature, and redox of the melt and by investigating the volatile contents. We also characterize the arc signature

found in the FSC and relate it to the local geodynamic settings. Further, by choosing suitable trace element ratios, we can trace the mantle component and study its variability along the back arc. Comparing the effects of different melting environments, subduction component, and mantle source allows us to establish a model of subduction-related melt generation and pathways, and mantle heterogeneity in the northeastern Lau Basin.
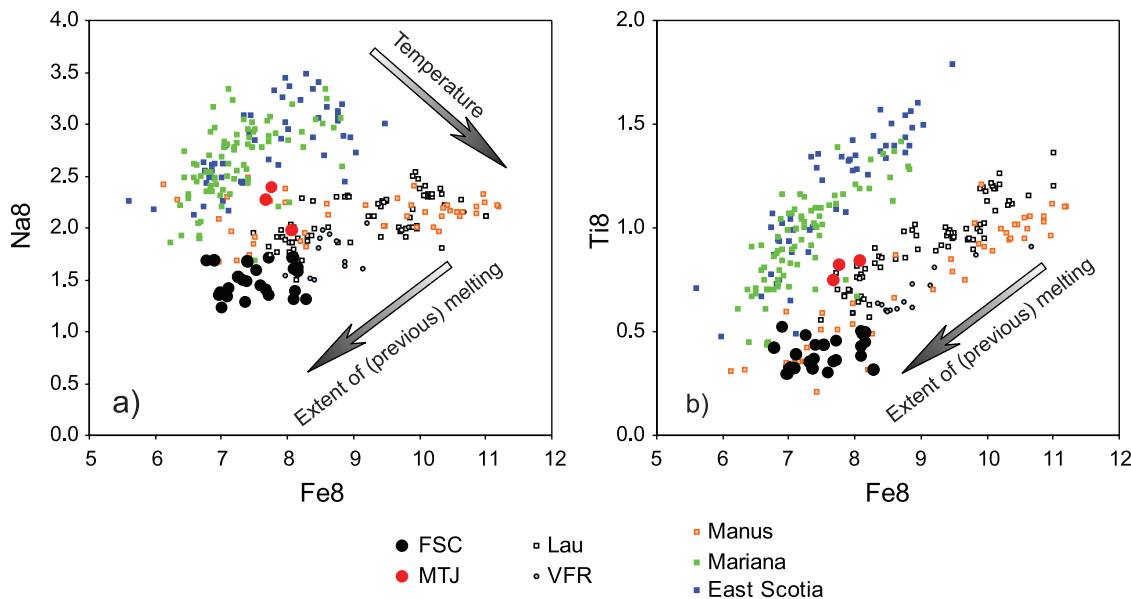
Figure 11. (a) Na8 versus Fe8, (b) Ti8 versus Fe8 for the FSC and MTJ samples (this study), compared with other back-arc basins. The following equations are used: Na8 = [Na$_2$O + 0.115(8 − MgO)]/[1 + 0.133(8 − MgO)]; Fe8 = [FeO$_{tot}$ + 8 − MgO]/[1 + 0.25(8 − MgO)]; Ti8 = (TiO$_2$)(MgO)1.7/34.3 [*Taylor and Martinez*, 2003, and references therein]. Data from other basins are taken from the compilation by *Taylor and Martinez* [2003] (East Scotia, Lau, Manus, Mariana) and R. J. Arculus (unpublished data set, 2007) (Valu Fa Ridge). Only samples with MgO > 5 wt% were used.
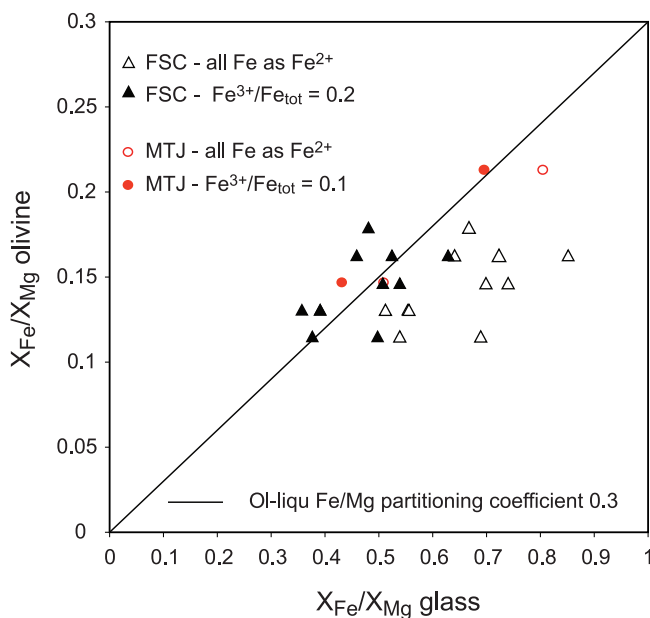
Figure 12. Plot of $[X_{Fe}/X_{Mg}]_{olivine}$ versus $[X_{Fe}/X_{Mg}]_{glass}$. Empty symbols represent uncorrected data (all Fe as Fe^{2+}) and filled symbols represent corrected data. The 0.3 equilibrium line is from *Roeder and Emslie* [1970].

5.1. Melting Environment of the Fonualei Spreading Center

5.1.1. Mantle Potential Temperature

[32] A relative estimate of the mantle potential temperature and extent of (previous) melting can be made using fractionation-corrected major element systematics. *Klein and Langmuir* [1987] pointed out that shallow level fractionation processes affect ridge basalt compositions and proposed a method to mitigate these fractionation effects to allow comparison of samples and sample suites: liquid lines of descent are calculated for low pressure fractionation of olivine, plagioclase, and clinopyroxene, and elemental abundances can be derived for a chosen MgO content [*Klein and Langmuir*, 1987; *Weaver and Langmuir*, 1990]. This approach was applied to BABB by *Taylor and Martinez* [2003] who recalculated a series of elements to 8 wt% MgO for various back-arc basins and showed that increasing mantle potential temperature leads to a decrease in Na8 and an increase in Fe8, whereas increasing extent of melting leads to a decrease in Fe8 and Ti8. We use the same equations as these authors. The equations are given in the caption of Figure 11. Only samples with MgO contents greater than 5 wt% were used, as lower MgO contents indicate that the samples have been affected by further fractionation. *Langmuir et al.* [2006] noted that in hydrous systems such as BABB, the melt evolution is different to the MORB environment due to the fact that water suppresses the appearance of plagioclase [*Green and Ringwood*, 1967]. The approach described by *Taylor and Martinez* [2003] is based on the assumption of crystallization of olivine, pyroxene, and plagioclase; thus the lack of plagioclase crystallization would affect the calculations of liquid lines of descent and may lead to low Fe8 and Ti8 values [*Asimow and Langmuir*, 2003; *Langmuir et al.*, 2006]. However, a majority of our samples contain plagioclase phenocrysts, which suggests that the water contents were low enough for the melt generated to be on a liquid line of descent generated by olivine, pyroxene, and plagioclase crystallization and the equations used are appropriate for this system.

[33] Figure 11 shows Na8 and Ti8 versus Fe8 for the FSC and the MTJ samples, together with samples from other locations (Mariana, East Scotia, Manus, and Lau basin (CLSC, ELSC, VFR)). The samples from the FSC form a low Na8, low Fe8, and low Ti8 end-member population, corresponding to a relatively high potential mantle temperature and high extent of previous melting, which is also the end-member characterized as most "arc-like" by *Taylor and Martinez* [2003]. The MTJ samples are similar to the bulk of the rest of the Lau Basin. The mantle wedge underlying the Lau basin has been inferred to be relatively hot due to the fast subduction rate, which induces fast mantle advection [*Peacock*, 1996]. This was also shown by anomalously low seismic velocities in the mantle wedge [*Wiens et al.*, 2006], as well as by calculations based on H_2O contents in the Lau BABB [*Kelley et al.*, 2006].

5.1.2. Temperature and Redox of the Melt

[34] Phenocryst data allow us to gain first-order estimates of temperature and redox conditions during melting. The coexistence of clinopyroxene and orthopyroxene in a few samples from FSC S and FSC CN enabled us to estimate the temperature of the melt. We used the pyroxene thermometer established by *Wells* [1977], which uses Ca, Mg, and Fe contents in coexisting clinopyroxene and orthopyroxene to derive the temperature of crystallization. Our results suggest temperatures between 1180 and 1230°C, which is slightly higher than previous estimates of the temperature of crystallization of the Tonga Arc [*Ewart*, 1976], consistent with the hot mantle potential temperatures inferred from this study.

[35] The forsterite content of olivine phenocrysts can be used to estimate the oxygen fugacity (fO_2) prevailing during crystallization. If olivine and melt are in equilibrium, experiments show that $[X_{Fe}/X_{Mg}]_{olivine} = 0.3 * [X_{Fe^{2+}}/X_{Mg}]_{melt}$ [*Roeder and Emslie*, 1970; *Toplis and Carroll*, 1995]. In a plot of $[X_{Fe}/X_{Mg}]_{olivine}$ versus $[X_{Fe}/X_{Mg}]_{melt}$, all data should plot on a line with slope 0.3 if all Fe in the melt is present as Fe^{2+}. If part of the Fe is present as Fe^{3+}, the data is shifted away from the 0.3 line; the extent of this shift can be used to constrain Fe^{3+}/Fe_{tot} in the melt (Figure 12). For the FSC, a correction of $Fe^{3+}/Fe_{tot} = 0.2$ is required in order for the samples to plot on a 0.3 slope, and the MTJ samples lie on the partitioning line with $Fe^{3+}/Fe_{tot} = 0.1$, indicating that the MTJ is generally more reduced than FSC. Fe^{3+}/Fe_{tot} ratios can then be linked to fO_2 using the algorithm of *Kilinc et al.* [1983]. The Fe^{3+}/Fe_{tot} of 0.2 in the FSC corresponds to an fO_2 about 0.5 log units above the synthetic fayalite-magnetite-quartz buffer (FMQ + 0.5), and in the case of the MTJ, Fe^{3+}/Fe_{tot} of 0.1 is about one log unit more reduced (FMQ-0.5). The MTJ value is consistent with the redox state of MORB [*Bezos and Humler*, 2005], and the more oxidized fO_2 found at the FSC is at the low end of the range for arcs FMQ + 0.5 to 3 [see *Parkinson and Arculus*, 1999].

5.1.3. Volatiles

[36] There is a marked difference in S and Cl contents between the FSC and the MTJ (see Figure 6). In the FSC
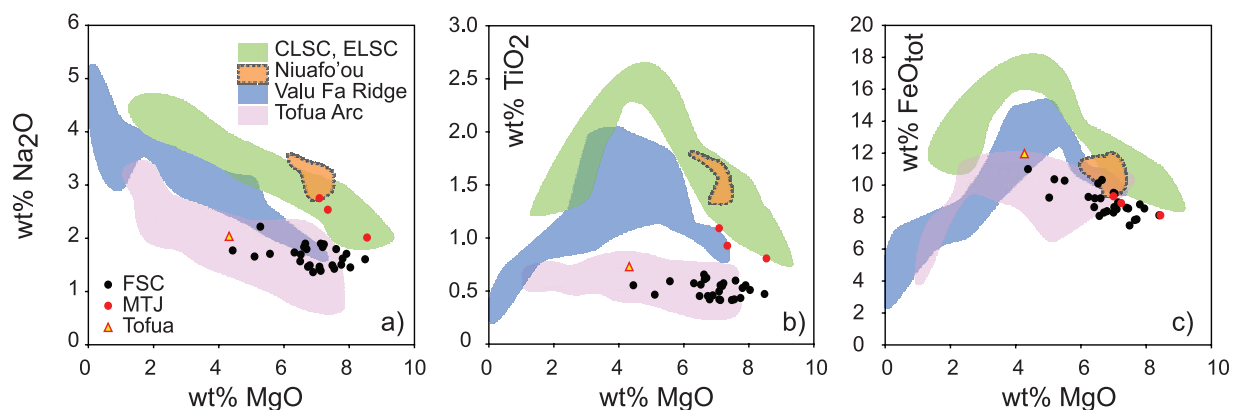
Figure 13. MgO variation diagrams for FSC, MTJ and Tofua, compared to other settings in the Tonga-Lau arc-back-arc system. (a) Na_2O versus MgO, (b) TiO_2 versus MgO, (c) FeO_{tot} versus MgO (all Fe as Fe^{2+}). CLSC and ELSC field from *Langmuir et al.* [2006] and VFR field from R. J. Arculus (unpublished data set, 2007) (cf. Figure 4); Niuafo'ou and Tofua Arc fields from GEOROC. All oxides recalculated to 100% anhydrous.

samples, S is low and Cl is high, whereas in the MTJ samples S is high and Cl is low. Degassing can affect volatiles contents, and the presence of vesicles in most of the samples indicates that although the samples were quenched under several thousands of meters of water, degassing still took place. However, there is no correlation between either Cl or S and vesicularity; therefore it is assumed that the samples generally retained their preeruptive Cl and S contents. This is consistent with a study by *Stroncik and Haase* [2004], which showed that Cl is not volatile at water depths greater than 400 m.

[37] In back arcs close to the arc, Cl is thought to be introduced into the mantle wedge by the subduction component [*Kent et al.*, 2002], as high Cl contents are found in the samples that have higher subduction signatures, such as Ba/Yb; at the MTJ the subduction component appears to be more dilute, which leads to lower Cl abundances. As is the case with other subduction tracers, there is no systematic correlation between Ba/Yb, Cl, and latitude.

[38] In the case of sulfur, there is a major difference between the samples from the MTJ (770–920 ppm S), which have values typical for MORB, and the FSC (30–160 ppm), which are strongly S depleted, up to ten times less than primitive mantle values. Given the lack of correlation between vesicularity and S content, degassing does not appear to be the main factor causing the observed difference in S contents between the MTJ and the FSC. A further efficient way of stripping S from the melt by fractionation of a mineral phase is by the formation of a sulfide phase. However, no correlation can be seen between S and Fe, which suggests that the melts were below sulfide saturation. Therefore it is expected that S behaves like an incompatible element and shows an increase with increasing fractionation. However, in the FSC the most fractionated samples are also the ones with the lowest S contents. There is no correlation between S and tracers from the slab (e.g., Ba/Yb), ruling out any cogenetic link. Other trace elements show that there is an increase in mantle depletion between the MTJ and the southernmost FSC (see Figure 9a), which is expected to affect S as well. This would be in agreement with the observation that S is highest in the least depleted

lavas. However, we find that mantle depletion indicators such as Nb/Yb vary steadily with latitude (see below), whereas sulfur values jump by a factor of 5 between FSC N and the MTJ. We attribute this sharp change in S content to the different redox conditions discussed above, as this is likely to strongly influence the behavior of S [*Carroll and Rutherford*, 1988; *Nilsson and Peach*, 1993; *Nilsson Farley*, 1994; *Clemente et al.*, 2004]. In a study of sulfur concentration in MORB and BABB glasses, *Nilsson and Peach* [1993] show that the sulfur contents can change from about 1500 ppm at NNO-1 to about 50 ppm at NNO + 1; This was also seen in experimental studies where sulfur encounters a solubility minimum around NNO + 1 [*Clemente et al.*, 2004]. Therefore the very sharp change that occurs over a horizontal distance a mere of 50 km could be explained by the presence, below the MTJ, of mantle that is about one log unit more reduced than the subarc mantle underlying the FSC. These results are again consistent with the observation that the samples from the MTJ have more MORB-like affinities than those from the FSC. A similar situation was found in the Mariana subduction system by *Alt et al.* [1993], where the back-arc samples (more MORB-like) show higher S than the arc samples; the authors also attributed the sulfur depletion in the arc to the more oxidizing conditions prevailing in the arc environment. The large difference in S contents between FSC and MTJ, which contrasts with the gradual decrease in mantle depletion documented by the HFSE, suggests that S is very strongly affected by redox, as opposed to HFSE. The strong redox control on S solubility has been shown in numerous studies [e.g., *Wallace and Carmichael*, 1992; *Nilsson Farley*, 1994; *Scaillet and Clemente*, 1998], and the change of sulfur speciation in the melt (sulfide at low fO_2 and sulfate at high fO_2) causes different solubility and degassing behavior.

5.2. Characterization of the Arc Signature: BABB or IAB?

5.2.1. Major Elements

[39] The FSC samples (excluding the MTJ samples) have very strong arc-like features. An example illustrating this is
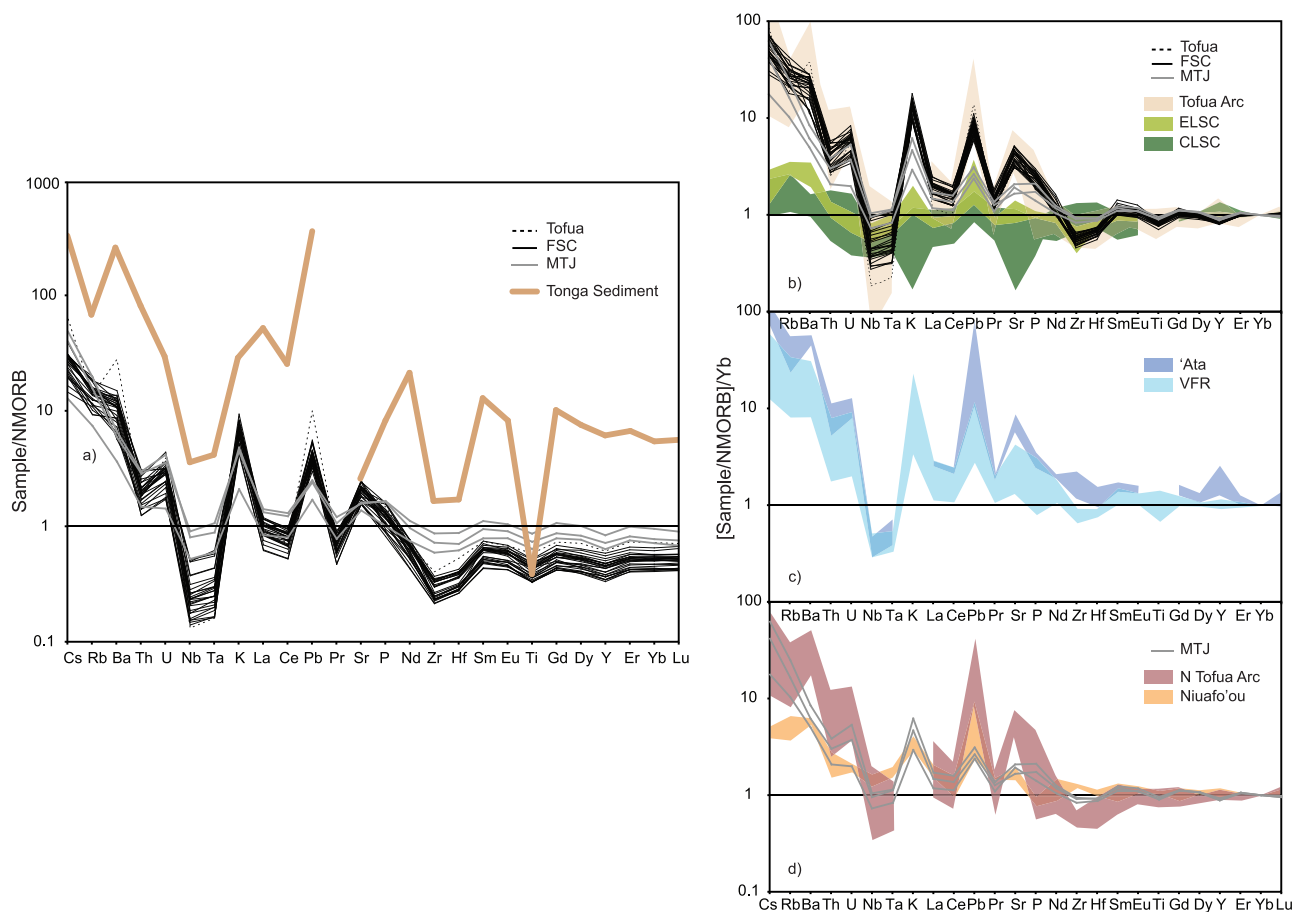
Figure 14. (a) N-MORB normalized data from this study (FSC, MTJ, and Tofua samples), with data for sediments being subducted at the Tonga trench [*Plank and Langmuir*, 1998]. (b) Yb-, N-MORB normalized data from this study, with fields for central Tofua Arc volcanoes (Hunga Tonga, Hunga Ha'apai, Metis Shoal, Tofua, Late, Fonualei) from the GEOROC compilation (cf. caption of Figure 10), and Lau Spreading Centers (ELSC, CLSC) from *Sun et al.* [2003] and the compilation by *Langmuir et al.* [2006]. (c) Yb-, N-MORB normalized Valu Fa Ridge samples (R. J. Arculus, unpublished data set, 2007), compared with the adjacent arc volcano 'Ata (GEOROC compilation). (d) Yb-, N-MORB normalized data from Northeast Lau basin: MTJ (this study), compared with fields for Niuafo'ou and North Tofua Arc volcanoes (Tafahi and Niuatoputapu) taken from the GEOROC compilation.

shown in Figure 13 where major element data is shown in comparison with data from the MORB-like Lau spreading ridges (CLSC, ELSC), the Valu Fa Ridge (VFR), and the Tofua Arc. For a given MgO, the MORB-like CLSC and ELSC have usually higher Na_2O, TiO_2, and FeO_{tot} than the Tofua Arc. The VFR typically plots in between Lau and Tofua Arc. The FSC samples mainly overlap with the Tofua Arc field, whereas the MTJ are shifted toward higher, more MORB-like values. In the case of Na_2O (Figure 13a), it can be seen that the FSC field overlaps with both the Tofua Arc and the VFR which has been argued to be an extreme case of arc-like BABB [e.g., *Fretzdorff et al.*, 2006].

5.2.2. Trace Elements

[40] Another useful way of evaluating the subduction signature in the context of the Lau Basin is by using N-MORB normalized incompatible element plots. The N-MORB normalized trace element data is shown in Figure 14 in the context of other locations in the Tonga–Lau system. Figure 14a shows that the general pattern of the FSC data

mimics that of the subducted sediments. The features of the sediment pattern are usually strongest in the Tofua sample and in the FSC samples and small or absent in the MTJ samples; this is the case for instance for Rb/Ba_{norm} and La/Ce_{norm}. When comparing the data with the Tofua Arc and the Lau spreading Centers (CLSC and ELSC), as seen in Figure 14b, the FSC samples are virtually indistinguishable from those from the Tofua Arc; only Ba is quite distinctly lower. The MTJ samples have less pronounced anomalies, and are shifted toward patterns that resemble Lau MORB. The FSC samples have very similar patterns and abundances to the VFR. However, in contrast to the FSC overlapping with the Tofua Arc, only few of the VFR data overlap with the field for the volcanic front (Figure 14c, subaerial lavas from 'Ata volcano, see Figure 1). Figure 14d shows samples from the northernmost area of the Lau-Tonga system, in a west-east transect: the MTJ samples are shown in comparison with the back-arc volcano Niua-
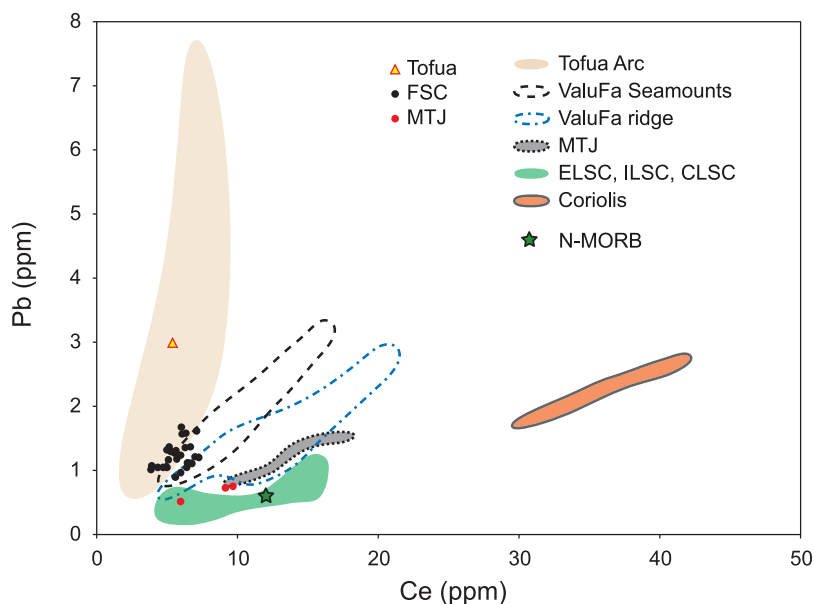
Figure 15. Pb versus Ce concentrations of the FSC, MTJ, and Tofua samples, compared with data for the Tofua Arc [*Ewart et al.*, 1998], Valu Fa Ridge, and seamounts (R. J. Arculus, unpublished data set, 2007), Lau Basin (CSLC, ILSC, ELSC) (compilation by *Langmuir et al.* [2006]), MTJ, and Coriolis Trough [*Sun et al.*, 2003]. N-MORB values from *Hofmann* [1988].

fo'ou which is further away from the arc, and the Tofua Arc volcanoes Tafahi and Niuatoputapu. The MTJ samples generally plot in between the two fields, consistent with changes in composition with distance to the arc [e.g., *Ewart et al.*, 1998]. Comparison of Figure 14d with Figures 14b and 14c also illustrate how HFSE depletion changes from south to north.

[41] A complementary proxy for subduction signature is Pb versus Ce [e.g., *Wendt et al.*, 1997; *Peate et al.*, 2001]. Pb and Ce are similarly incompatible during mantle melting, and N-MORB has a Pb/Ce ratio around 0.04 [*Hofmann*, 1988], increasing with additional subduction input [*Miller et al.*, 1994]. This enrichment in Pb relative to Ce is usually attributed to higher Pb solubility than Ce in aqueous fluids [*Brenan et al.*, 1995]. Figure 15 shows Pb versus Ce for the FSC, with fields representing other locations for comparison. The Pb/Ce of the FSC generally overlaps with the Tofua Arc, which have Pb/Ce of 0.5–1. This range matches the Pb/Ce ratio of the subducted sediment (0.6) [*Plank and Langmuir*, 1998], showing a very strong input from the subduction zone. The FSC samples are similar to the VFR seamounts samples, which show stronger arc affinities than the ridge itself, consistent with the fact that they are closer to the arc than the ridge is. The VFR ridge samples are transitional between the arc and the southern Lau spreading centers (ELSC, ILSC, CLSC). The MTJ samples are similar
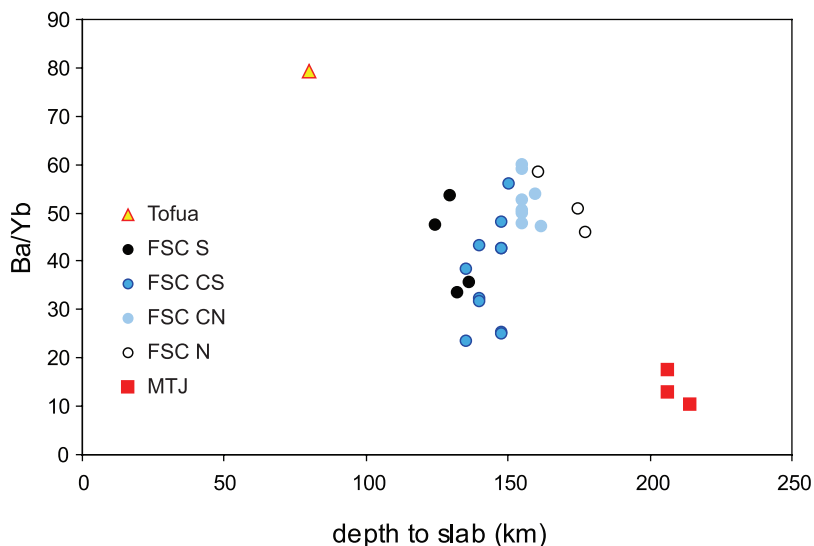

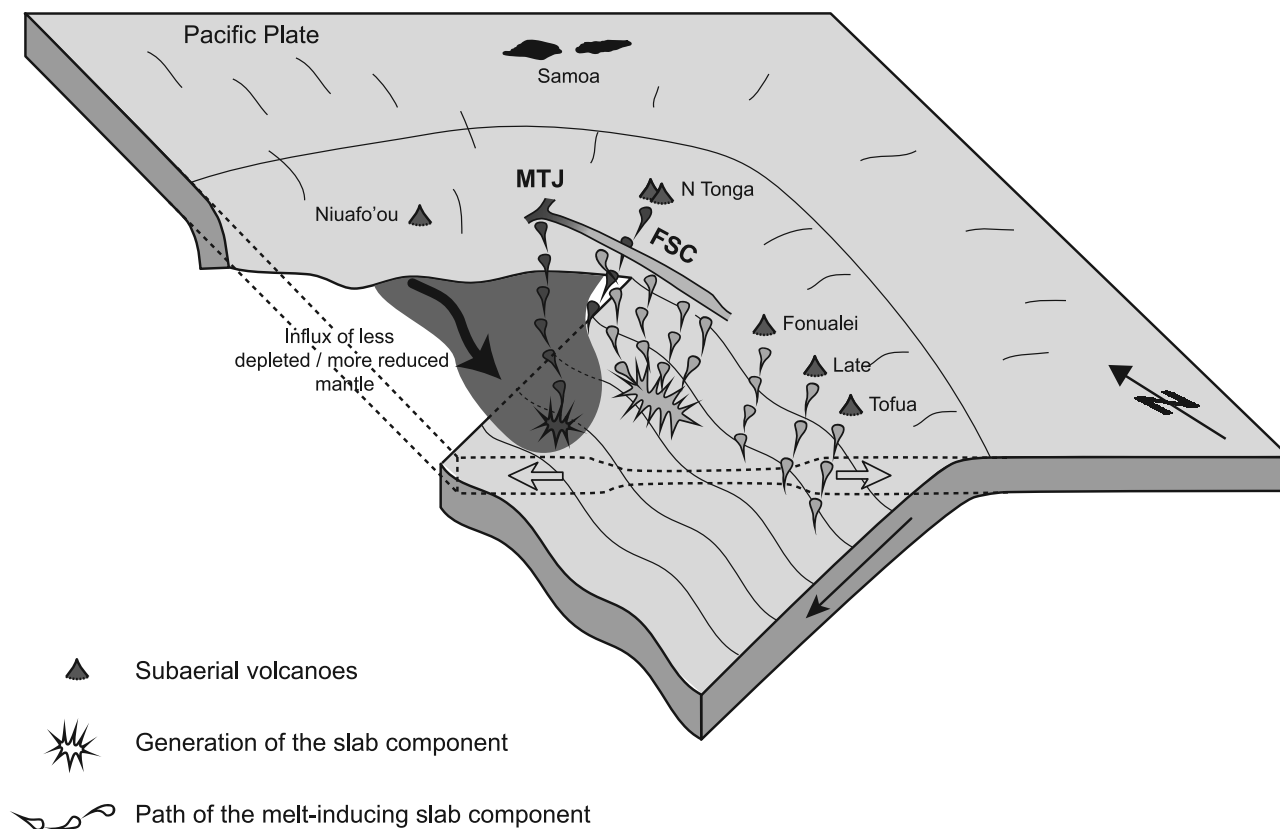**Figure 16.** Ba/Yb versus depth to the top of the slab for the FSC, MTJ, and Tofua samples. Abbreviations as in Figure 3b.

Figure 17. Nb/Yb versus latitude for the FSC, MTJ, and Tofua samples. Abbreviations as in Figure 3b.

to the southern spreading centers, with Pb/Ce that are consistent with N-MORB; the Coriolis Troughs, another nascent back-arc basin adjacent to the southern New Hebrides Arc with N-MORB characteristics [*Sun et al.*, 2003], have similar ratios, yet higher absolute abundances.

[42] A number of authors [e.g., *Stern et al.*, 1990; *Hochstaedter et al.*, 2001; *Portnyagin et al.*, 2007] have argued that the subduction signature changes with increasing depth to the slab. Figure 16 shows a subduction tracer ratio, Ba/Yb, versus depth to the slab as inferred from our 3-D slab reconstructions. Figure 16 shows that at the scale of the entire system from the arc (Tofua) to the MTJ, the Ba/Yb ratios are generally controlled by the depth to the slab, with the main geochemical divides situated between the MTJ and the northernmost FSC sample (dredge 67, Figure 3b), and between the southernmost FSC sample (dredge 47, Figure 3b) and Tofua. However, if only the samples within the FSC are considered, Figure 16 (coupled with the geochemical maps shown earlier in Figures 9a and 9b) illustrates that while there is a relatively large variation of the subduction component, it is not systematic. Yet the depth to the slab increases by 50 km from the southern most FSC sample to the northernmost one. This indicates that the plumbing system below the FSC is intricate and the erupted lavas were probably not generated vertically beneath the locus of their eruption. The lack of systematic correlation between depth to the slab and subduction tracers may indicate that magma generation occurs at a single depth and that the generated melts follow zones of weakness provided by spreading. This in turn implies that the generally observed changes in geochemistry with depth to the slab do not necessarily apply for small-scale, complex geometries as encountered at the FSC.

5.2.3. Arc Shutoff

[43] The combined results of major and trace elements show that the FSC sample suite appears to have a stronger subduction signature when compared to samples from most other back-arc basins. In particular, the FSC has more affinities to the central and northern Tofua arc than VFR

does to 'Ata, despite the fact that VFR is in a similar setting to the FSC in its proximity to the volcanic arc front. A notable difference between VFR and FSC is that VFR is erupting basaltic to felsic magmas, whereas FSC only erupts basalts and andesites. This may be linked to the fact that VFR is currently in a rifting mode [*Fretzdorff et al.*, 2006], whereas FSC is in spreading mode. The nature and the timing of the transition between IAB-like and MORB-like geochemical affinities in back-arc basins remain uncertain. Some authors have suggested that the change occurs with the maturity of the system [e.g., *Saunders and Tarney*, 1979; *Hawkins and Melchior*, 1985]. According to these studies, the lavas erupted at the onset of rifting are arc-like, with melting processes dominated by fluid fluxing. As the system evolves and the back arc migrates away from the arc, the petrogenetical processes change to be more MORB-like (combination of flux and decompression melting [e.g., *Gribble et al.*, 1996]). The trace element signature in the BABB is then attributed to metasomatism in the mantle wedge (e.g., North Marianas) [*Stern et al.*, 1990]. Other authors have shown that even the very first melts to be generated in a nascent back arc have BABB characteristics, distinct from their adjacent arc (e.g., Sumisu Rift) [*Fryer et al.*, 1990].

[44] In the case of Lau, at the scale of the entire basin it appears that the younger, more arc proximal centers are more arc-like (VFR, *Fretzdorff et al.* [2006], and FSC, this study) whereas the older, more distal spreading centers are more MORB-like, with true BABB characteristics (ELSC, CLSC [e.g., *Pearce et al.*, 1995]). On a smaller scale, there is a distinction between the VFR, which is currently producing BABB, and the FSC, which is producing IAB. Although VFR and FSC are similar in their proximity to the volcanic arc front, the arc adjacent to Valu Fa appears to be active, as shown by the numerous seamounts to the east of the ridge [*Arculus et al.*, 2003] and 'Ata, which is inferred to be between 10 and 100 ka [*Turner et al.*, 1997]. On the other hand, the arc adjacent to the FSC appears to be shut off, as shown in Figure 3a and discussed earlier. This is a

Figure 18. Three-dimensional model of the northeast Lau Basin, showing the geometry of the subducting Pacific Plate, with the tear through which less depleted mantle flows in from the north. Relative depths of generation of the subduction component in the FSC and MTJ, as well as inferred paths of this component, are shown; this component feeds the arc volcanoes south and north of the FSC and is captured by the FSC in between, as the adjacent submarine volcanoes are shut off. Basic geometry from *Turner and Hawkesworth* [1998].

situation comparable to the Mariana subduction system, which was described by *Gribble et al.* [1998]. In the case of the Mariana Arc, the arc volcanoes in the area where the back-arc basin is closest to the arc (30–100 km horizontal distance) are currently inactive. The back-arc basalts from this area are geochemically indistinguishable from the volcanic arc, and the authors conclude that all the flux from the subduction zone is captured into the back arc. Similarly, in the case of the FSC there is no reason for the flux from the subducting Pacific Plate into the overlying mantle to cease, and the melts generated by flux melting in the mantle wedge appear to have been totally captured by the FSC. An enhanced "subduction zone signature" in the FSC compared with other back-arc systems adjacent to active arc volcanism is therefore be expected. The VFR might be in a similar setting to the Sumisu Rift [*Fryer et al.*, 1990; *Hochstaedter et al.*, 1990] where the initial melts are BABB as opposed to IAB; in these two cases, the adjacent arc is active, suggesting that there are separate melt pathways for the arc and for the back arc.

[45] Additionally, it is noteworthy that the FSC is close enough to the adjacent volcanic arc that it lies at a depth over the subducted slab which is typical for arc volcanism. The depth to the slab beneath the FSC ranges from 120 to 220 km, which overlaps estimates for global arcs by

England et al. [2004] (65–130 km) and *Syracuse and Abers* [2006] (72–173 km). The range for the FSC is thus shallower than that of other BABB, in particular the other back-arc spreading centers in the Lau Basin such as the ELSC and the CLSC (depth to the slab 150–300 km [*Martinez and Taylor*, 2002]). This is likely to be another factor controlling the generation of arc-like melts.

5.3. Geochemical Changes With Latitude: Mantle Component

[46] Generally, across the Lau Basin, the mantle wedge becomes gradually more depleted from south to north (due to increased spreading in the north) and from west to east (continuous depletion of the west-east mantle migration due to corner flow) [e.g., *Ewart et al.*, 1998]. In the case of the FSC, a different trend is observed, as illustrated by Figure 17, which shows Nb/Yb versus latitude. While the FSC is more depleted (also further east/closer to the arc) than the MTJ, the mantle depletion decreases from south to north (see also Figure 7b and Figure 9a). The change in depletion signature is relatively gradual, as opposed to the subduction signatures which were distinctive by their lack of trend with latitude within the FSC; this shows that it is truly a mantle signature, and not a subduction signature. It has been noted in previous studies [*Volpe et al.*, 1988; *Wendt et al.*, 1997;

Ewart et al., 1998; *Turner and Hawkesworth*, 1998] that the northernmost volcanoes of the Tofua Arc (Tafahi and Niuatoputapu) as well as the back-arc island of Niuafo'ou show a distinctively less depleted mantle signature than the rest of the arc. The MTJ samples are generally less depleted than the FSC samples, similar to Niuafo'ou and the northern volcanoes (Figure 14d). This can be attributed either to the longer depletion history of the mantle closer to the subduction zone or to potential influx of more fertile mantle around the edge of the northern slab boundary, through a tear in the Pacific Plate [*Millen and Hamburger*, 1998]. The latter was suggested for the northernmost islands of the arc, Tafahi and Niuatoputapu [*Wendt et al.*, 1997; *Turner and Hawkesworth*, 1998]; it is most likely a combination of both processes.

[47] Isotope geochemical studies [e.g., *Volpe et al.*, 1988; *Hergt and Hawkesworth*, 1994; *Pearce et al.*, 1995; *Wendt et al.*, 1997; *Ewart et al.*, 1998; *Turner and Hawkesworth*, 1998; *Falloon et al.*, 2007; *Pearce et al.*, 2007] suggest that the mantle wedge underlying the Lau Basin is heterogeneous, as a result of a complex tectonic history. However, the origin of these signatures, their distribution and even definition are still under debate (compare Figure 1 in the work of *Turner and Hawkesworth* [1998] with Figure 7 in the work of *Pearce et al.* [2007]). The new data on S abundances and redox of the melt constrained by Fe ratios in olivine suggests the presence of two different mantle sources below the MTJ and the FSC, with a more reduced mantle closer to the tear.

[48] The sharp geochemical contrast between the FSC and the MTJ samples could indicate that there is a change in mantle provenance between the northernmost FSC N dredge (67) and the MTJ, at least at the locus of the generation of their parental melts, with more depleted mantle wedge feeding the FSC, whereas the mantle wedge below MTJ is more reduced and less depleted, possibly flowing in southward through a tear in the Pacific Plate, at the northern boundary of the Lau Basin [*Turner and Hawkesworth*, 1997; *Millen and Hamburger*, 1998]. This would be consistent with the conclusions by *Turner and Hawkesworth* [1998] based on isotopic work, who place the boundary between two mantle domains just south of the MTJ.

[49] Alternatively, the difference in geochemistry between the FSC and the MTJ could be explained through fundamentally different melt sources and melting processes due to different depth to the slab, distance to the arc, and mantle wedge depletion. In particular, based on the sulfur systematics, the Fonualei Spreading Center reflect oxidized, arc-like melts, whereas the MTJ shows MORB-like, more reduced character, similar to what was suggested by *Alt et al.* [1993] (Mariana Arc) and *Nilsson Farley* [1994] (Lau Basin).

[50] The two options do not need to be mutually exclusive; further work is needed to determine the extent of each contribution, in particular by investigation of the isotopic systematics.

5.4. Model of Petrogenesis in NE Lau Basin

[51] Following synthesis of observations enable us to propose a 3-D model of the interaction between subduc-tion-derived component and mantle heterogeneity of the Fonualei Spreading Center region.

[52] 1. The FSC samples consist mainly of arc-like basaltic andesites, virtually indistinguishable in their major and trace element geochemistry from the adjacent Tofua Arc, suggesting that the petrogenesis for both settings is similar, and all the subduction flux is captured in the back arc.

[53] 2. Within the FSC, no trend can be seen in classic subduction tracers (e.g., Ba/Yb, Ba/La) versus depth to the slab, despite the fact that there is an increase in depth to the slab of 50 km between FSC S and FSC N, suggesting that the subduction component is released at the same depth.

[54] 3. There is a sharp contrast between the FSC and the MTJ. The MTJ is more MORB-like than the FSC. The MTJ appears to be more reduced mantle, based on higher sulfur contents and estimates of fO_2 using olivine-melt equilibrium. This might either indicate a change in mantle source, or reflect different geodynamic conditions of melt generation, or both.

[55] 4. The mantle depletion decreases steadily from south to north, in contrast to the general trend of the Lau Basin. This suggests the influx of less depleted mantle through the tear on the north.

[56] Figure 18 shows a cartoon of the region, which accommodates all the above observations. We suggest that the release of the subduction component in the FSC occurred at the same depth and followed different pathways to the surface with different length (in time and path) of interaction with the mantle; the melting process generating the FSC lavas is dominated by flux melting of the hot mantle wedge, and the slab component dilutes the geochemical signal expected from decompression melting generally thought to occur in back-arc basins. The single depth of subduction component origin explains the lack of systematic changes in subduction tracers with depth to the slab. The mantle signature, which changes steadily with latitude, is only visible in elements that are not present in the subduction component, such as Nb, Ta, and HREE. We also suggest that while there is no clear Samoa input into the MTJ, we do see a different mantle signature, and argue that there might be a boundary in mantle domains just south of the MTJ, between sampling site 67 and 70, as suggested by *Turner and Hawkesworth* [1998] (see their Figure 3).

6. Conclusions

[57] Major, volatile, and trace elements of glassy rims of pillow lavas dredged from a nascent spreading system show that the erupted lavas are geochemically indistinguishable from the adjacent volcanic arc and do not have the usual BABB characteristics. We attribute this to the proximity of the back arc to the arc, which has enabled the subduction flux to be captured by the back arc. No systematic change in subduction signature can be seen with depth to the slab, indicating that at this scale the assumption of geochemical changes with arc proximity do not apply. This is likely to be due to the subduction flux component being generated at one unique depth and following different pathways dependent on the local stress regime. The samples from the Mangatolu Triple Junction have BABB characteristics tran-
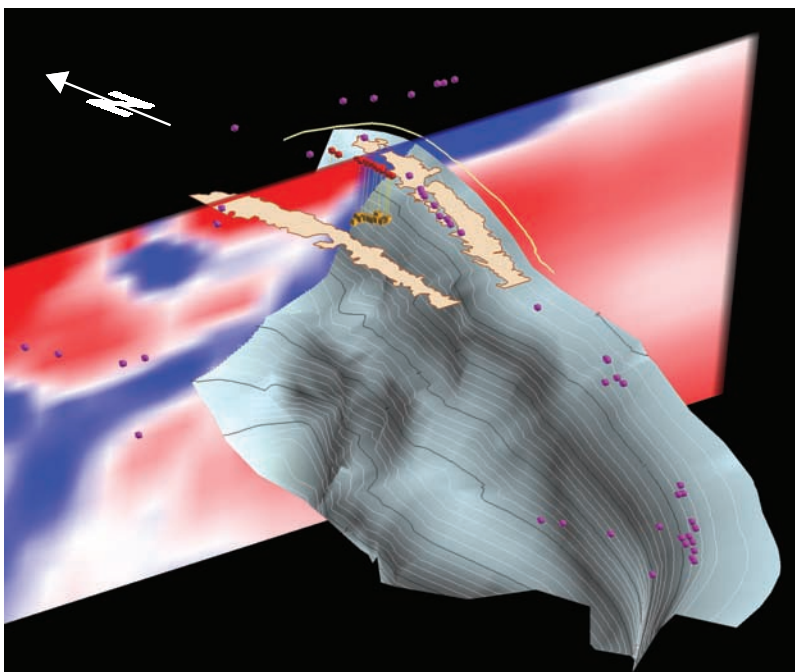
Figure A1. Example of a tomographic section used for the plate reconstruction. Blue and red colorations of the cross sections correspond to positive (max +1.191) and negative (min −1.326) perturbations in the velocity relative to the ak135 reference model [*Kennett et al.*, 1995]. White corresponds to transitional velocities of approximately +0.1. Symbols and contours as in Figure 2.

sitional between N-MORB (e.g., CLSC) and IAB (e.g., northern Tonga volcanoes). In particular, they appear to be more reduced than the oxidized arc-like FSC samples, which could be due to either (or a combination of) different melting processes (flux melting versus decompression melting) or to a different mantle origin. Unlike the general trend of gradual mantle wedge depletion from south to north observed at the scale of the Lau basin, the Fonualei Spreading Center show an increase in HFSE relative to N-MORB, suggesting the influx of less depleted mantle from the north.

Appendix A: Constructing the Virtual Earth—Geometry of the Tonga Slab

[58] Key to visualization of the Tonga Slab (subducted Mesozoic Pacific Plate) is the systematic delineation of its morphology using multiple data sources including earthquake hypocenter data (see below) and P wave tomography provided by *Widiyantoro et al.* [1999] and as presented by *Van Der Hilst et al.* [1997]. Several previously published slab models have used earthquake hypocenter data to define slab geometries [*Gutscher et al.*, 1999; *Rietbrock and Haberland*, 2001]. Data used by us to interpret the geometry of the Tonga Slab have been obtained from two sources: the EHB hypocenter catalog [*Engdahl et al.*, 1998] and the USGS National Earthquake Information Center (NEIC) earthquake hypocenter database (earthquakes > 4.0) for the time period between 1990 and 2005. Earthquake hypocenters were used to define the slab to depths of approximately 670 km. The data have been systematically analyzed in closely spaced sequential cross sections as well as in

interactive 3-D mode using the 3-D data visualization package EarthDecision Suite™ (Gocad v.2.1.6).

[59] In detail, the morphology of the subducted Tonga Slab and overlying Australian Plate has been interpreted between 33°S and 13°S. The slab geometry presented here was obtained by entering hypocenter data (X, Y, and Z) into both flat and spherical 3-D "Virtual Earth" models. The Tonga model was examined in over 40 adjacent E−W oriented cross-sections through the P wave tomographic model and earthquake hypocenter data that extended between the latitudes listed above and to a maximum depth of 1300 km. In addition, 24 north-south trending sections and 20 horizontal sections were also used in the interpretation. Additionally, 12 horizontal slices were selected for various depths in which the earthquake data were contoured according to the number/density of earthquakes within either 1×1 or 0.25×0.25 degree (lat-long) sampling grids. The method was applied to the global earthquake hypocenter data set at these depths. Utilizing the combination of methods described above has enabled us to define the geometry of the subducted plate to a depth of approximately 670 km. We assume that if the subducted slab is a relatively uniform subducting sheet of oceanic lithosphere, the outer (western) limit of the contoured earthquake hypocenters at depth should closely define the upper surface of the subducted slab (Figure 2a shown earlier).

[60] We also assume that earthquakes > ∼50 km depth are focused within the subducting slab [cf. *Cahill and Isacks*, 1992]. Previous studies incorporating earthquake and tomography show earthquake hypocenters corresponding with the top of the subducting slab at shallow depths but within

the core of the slab at depths of around 200 km [*Zhang et al.*, 2004; *Miller et al.*, 2006]. It is assumed that this variation is due primarily to thermal lag and associated delays in temperature-dependent phase changes experienced by the core of the slab during subduction. We have considered this feature in our comparisons of tomography and hypocenter data.

[61] A continuous irregularly tessellated 3-D surface was constructed so that it passes across the outer (western) limit of the contoured earthquake data and the western limit of the dense earthquake clusters interpreted to be contained within the slab. Numerous earthquake hypocenters exist in the mantle wedge above the northern Tonga Slab, but these were not included in the slab interpretation as they are typically single hypocenters located in scattered positions throughout the wedge. The position of the individual nodes was adjusted manually such that the surface encompasses the limits of the contoured earthquakes. The mesh surface that blankets the earthquake hypocenter data represents an initial slab geometry that is subsequently modified according to details observed in the corresponding tomography described below.

[62] To better constrain the geometry of the slab, especially at depth, we combined the 3-D analysis of earthquake data described above with selected regional P wave tomographic data sets. These data were plotted as variations in P wave travel time perturbations from the *ak135* velocity reference model [*Kennett et al.*, 1995]. Figure A1 shows an example of a cross section taken through the 3-D geophysical data set. In the slab model presented here, we have shown only the interpreted section of the slab above 670 km depth. Complexities in mantle structure to the west of the Tonga Slab such as slab fragments have not been included.

[63] In interpreting the position and geometry of the slab from the 3-D P wave tomography data set we have used the location of the highest positive anomaly observed in the P wave tomography at any given depth. At shallow levels (<100 km), the fastest positive velocity anomaly will delineate a surface that approximately defines the top of the slab but with depth, the anomaly should ultimately define a surface that more closely represents the slab core due to the delayed thermal equilibration described above. Although complications exist when interpreting images derived from color scaling tomographic model data, we have selected these criteria on the basis that the slab is coldest in its core and should, therefore, exhibit velocities that are defined by a positive perturbation from the surrounding mantle values. This characteristic is also shown by *Zhao and Kayal* [2000] where below approximately 50 km depth, the core of the slab is defined by the greatest positive perturbation in their tomography.

References

Alt, J. C., W. C. Shanks, and M. C. Jackson (1993), Cycling of sulfur in subduction zones: The geochemistry of sulfur in the Mariana-Island Arc and back-arc trough, *Earth Planet. Sci. Lett.*, 119, 477–494, doi:10.1016/0012-821X(93)90057-G.

Arculus, R. J. (2004), R.V. *Southern Surveyor* SS11/2004 NoToVE voyage summary, Commonw. Sci. and Ind. Res. Org., Melbourne, Victoria, Australia.

Arculus, R. J., et al. (2003), R/V *Southern Surveyor* 02/2003 Tonga-Eastern Lau Vents Expedition, March 14–April 3 2003 cruise report, Commonw. Sci. and Ind. Res. Org., Melbourne, Victoria, Australia.

Asimow, P. D., and C. H. Langmuir (2003), The importance of water to oceanic mantle melting regimes, *Nature*, 421, 815–820, doi:10.1038/nature01429.

Bevis, M., et al. (1995), Geodetic observations of very rapid convergence and back-arc extension at the Tonga Arc, *Nature*, 374, 249–251, doi:10.1038/374249a0.

Bezos, A., and E. Humler (2005), The Fe^{3+}/Sigma Fe ratios of MORB glasses and their implications for mantle melting, *Geochim. Cosmochim. Acta*, 69, 711–725, doi:10.1016/j.gca.2004.07.026.

Brenan, J. M., H. F. Shaw, and F. J. Ryerson (1995), Experimental-evidence for the origin of lead enrichment in convergent-margin magmas, *Nature*, 378, 54–56, doi:10.1038/378054a0.

Cahill, T., and B. L. Isacks (1992), Seismicity and shape of the subducted Nazca Plate, *J. Geophys. Res.*, 97, 17,503–17,529, doi:10.1029/92JB00493.

Carroll, M. R., and M. J. Rutherford (1988), Sulfur speciation in hydrous experimental glasses of varying oxidation-state - Results from measured wavelength shifts of sulfur X-rays, *Am. Mineral.*, 73, 845–849.

Clemente, B., B. Scaillet, and M. Pichavant (2004), The solubility of sulphur in hydrous rhyolitic melts, *J. Petrol.*, 45, 2171–2196, doi:10.1093/petrology/egh052.

de Ronde, C. E. J., E. T. Baker, G. J. Massoth, J. E. Lupton, I. C. Wright, R. A. Feely, and R. R. Greene (2001), Intra-oceanic subduction-related hydrothermal venting, Kermadec volcanic arc, New Zealand, *Earth Planet. Sci. Lett.*, 193, 359–369, doi:10.1016/S0012-821X(01)00534-9.

de Ronde, C. E. J., K. Faure, C. J. Bray, D. A. Chappell, and I. C. Wright (2003), Hydrothermal fluids associated with seafloor mineralization at two southern Kermadec arc volcanoes, offshore New Zealand, *Miner. Deposita*, 38, 217–233.

Eggins, S. M., and J. M. G. Shelley (2002), Compositional heterogeneity in NIST SRM 610–617 glasses, *Geostand. Newsl.*, 26, 269–286, doi:10.1111/j.1751-908X.2002.tb00634.x.

Elliott, T., T. Plank, A. Zindler, W. White, and B. Bourdon (1997), Element transport from slab to volcanic front at the Mariana arc, *J. Geophys. Res.*, 102, 14,991–15,019, doi:10.1029/97JB00788.

Engdahl, E. R., R. van der Hilst, and R. Buland (1998), Global teleseismic earthquake relocation with improved travel times and procedures for depth determination, *Bull. Seismol. Soc. Am.*, 88, 722–743.

England, P., R. Engdahl, and W. Thatcher (2004), Systematic variation in the depths of slab beneath arc volcanoes, *Geophys. J. Int.*, 156, 377–408, doi:10.1111/j.1365-246X.2003.02132.x.

Ewart, A. (1976), Petrological study of younger Tongan andesites and dacites, and olivine tholeiites of Niua-Foou Island, SW Pacific, *Contrib. Mineral. Petrol.*, 58, 1–21, doi:10.1007/BF00384740.

Ewart, A., K. D. Collerson, M. Regelous, J. I. Wendt, and Y. Niu (1998), Geochemical evolution within the Tonga-Kermadec Lau arc back-arc systems: The role of varying mantle wedge composition in space and time, *J. Petrol.*, 39, 331–368, doi:10.1093/petrology/39.3.331.

Falloon, T. J., A. Malahoff, L. P. Zonenshain, and Y. Bogdanov (1992), Petrology and geochemistry of back-arc basin basalts from Lau Basin spreading ridges at 15°, 18° and 19°S, *Mineral. Petrol.*, 47, 1–35, doi:10.1007/BF01165295.

Falloon, T. J., L. V. Danyushevsky, T. J. Crawford, R. Maas, J. D. Woodhead, S. M. Eggins, S. H. Bloomer, D. J. Wright, S. K. Zlobin, and A. R. Stacey (2007), Multiple mantle plume components involved in the petrogenesis of subduction-related lavas from the northern termination of the Tonga Arc and northern Lau Basin: Evidence from the geochemistry of arc and backarc submarine volcanics, *Geochem. Geophys. Geosyst.*, 8, Q09003, doi:10.1029/2007GC001619.

Fretzdorff, S., U. Schwarz-Schampera, H. L. Gibson, C. D. Garbe-Schonberg, F. Hauff, and P. Stoffers (2006), Hydrothermal activity and magma genesis along a propagating back-arc basin: Valu Fa Ridge (southern Lau Basin), *J. Geophys. Res.*, 111, B08205, doi:10.1029/2005JB003967.

Fryer, P., J. M. Sinton, and J. A. Philpotts (1981), Basaltic glasses from the Mariana Trough, in *Initial Reports of the Deep Sea Drilling Project*,

vol. 60, edited by D. M. Hussong and S. Uyeda, pp. 601–609, U.S. Govt. Print. Off., Washington, D. C.

Fryer, P., B. Taylor, C. H. Langmuir, and A. G. Hochstaedter (1990), Petrology and geochemistry of lavas from the Sumisu and Torishima backarc rifts, *Earth Planet. Sci. Lett.*, *100*, 161–178, doi:10.1016/0012-821X(90)90183-X.

German, C. R., E. T. Baker, D. P. Connelly, J. E. Lupton, J. Resing, R. D. Prien, S. L. Walker, H. N. Edmonds, and C. H. Langmuir (2006), Hydrothermal exploration of the Fonualei Rift and Spreading Center and the Northeast Lau Spreading Center, *Geochem. Geophys. Geosyst.*, *7*, Q11022, doi:10.1029/2006GC001324.

Gill, J. B. (1976), Composition and age of Lau Basin and ridge volcanic-rocks - Implications for evolution of an interarc basin and remnant arc, *Geol. Soc. Am. Bull.*, *87*, 1384–1395, doi:10.1130/0016-7606(1976)87<1384: CAAOLB>2.0.CO;2.

Govindaraju, K. (1994), 1994 compilation of working values and samples description for 383 geostandards, *Geostand. Newsl.*, *18*, 158 pp.

Green, D. H., and A. E. Ringwood (1967), The genesis of basaltic magmas, *Contrib. Mineral. Petrol.*, *15*, 103–190, doi:10.1007/BF00372052.

Gribble, R. F., R. J. Stern, S. H. Bloomer, D. Stuben, T. O. Hearn, and S. Newman (1996), MORB mantle and subduction components interact to generate basalts in the southern Mariana Trough back-arc basin, *Geochim. Cosmochim. Acta*, *60*, 2153–2166, doi:10.1016/0016-7037(96)00078-6.

Gribble, R. F., R. J. Stern, S. Newman, S. H. Bloomer, and T. O'Hearn (1998), Chemical and isotopic composition of lavas from the Northern Mariana Trough: Implications for magmagenesis in back-arc basins, *J. Petrol.*, *39*, 125–154, doi:10.1093/petrology/39.1.125.

Gutscher, M. A., J. L. Olivet, D. Aslanian, J. P. Eissen, and R. Maury (1999), The "lost Inca Plateau": Cause of flat subduction beneath Peru?, *Earth Planet. Sci. Lett.*, *171*, 335–341, doi:10.1016/S0012-821X(99)00153-3.

Hamburger, M. W., and B. L. Isacks (1988), Diffuse back-arc deformation in the southwestern Pacific, *Nature*, *332*, 599–604, doi:10.1038/332599a0.

Hart, S. R., D. E. Karig, and W. E. Glassley (1972), Basalts and sea-floor spreading behind Mariana Island Arc, *Earth Planet. Sci. Lett.*, *15*, 12–18, doi:10.1016/0012-821X(72)90023-4.

Hawkins, J. W. (1995), The geology of the Lau Basin, in *Backarc Basins: Tectonics and Magmatism*, pp. 63–138, edited by B. Taylor, Plenum, New York.

Hawkins, J. W., and J. T. Melchior (1985), Petrology of Mariana Trough and Lau Basin basalts, *J. Geophys. Res.*, *90*, 11,431–11,468, doi:10.1029/JB090iB13p11431.

Hergt, J., and C. Hawkesworth (1994), Pb-, Sr-, and Nd-isotopic evolution of the Lau Basin: Implications for mantle dynamics during back-arc opening, in *Proc. Ocean Drill. Program Sci. Results*, vol. 135, edited by J. Hawkins et al., pp. 505–517, Ocean Drill. Program, College Station, Tex.

Hermann, J., C. Spandler, A. Hack, and A. V. Korsakov (2006), Aqueous fluids and hydrous melts in high-pressure and ultra-high pressure rocks: Implications for element transfer in subduction zones, *Lithos*, *92*, 399–417, doi:10.1016/j.lithos.2006.03.055.

Hochstaedter, A. G., J. B. Gill, and J. D. Morris (1990), Volcanism in the Sumisu Rift. 2. Subduction and non-subduction related components, *Earth Planet. Sci. Lett.*, *100*, 195–209, doi:10.1016/0012-821X(90)90185-Z.

Hochstaedter, A., J. Gill, R. Peters, P. Broughton, P. Holden, and B. Taylor (2001), Across-arc geochemical trends in the Izu-Bonin arc: Contributions from the subducting slab, *Geochem. Geophys. Geosyst.*, *2*(7), 1019, doi:10.1029/2000GC000105.

Hofmann, A. W. (1988), Chemical differentiation of the Earth - The relationship between mantle, continental-crust, and oceanic-crust, *Earth Planet. Sci. Lett.*, *90*, 297–314, doi:10.1016/0012-821X(88)90132-X.

Ihinger, P. D., R. L. Hervig, and P. F. McMillan (1994), Analytical methods for volatiles in glasses, in *Volatiles in Magmas*, *Rev. in Mineral.*, vol. 30, edited by M. R. Carroll and J. R. Holloway, pp. 67–121, Mineral. Soc. of Am., Washington, D. C.

Johnson, M. C., and T. Plank (1999), Dehydration and melting experiments constrain the fate of subducted sediments, *Geochem. Geophys. Geosyst.*, *1*(1), 1007, doi:10.1029/1999GC000014.

Kelley, K. A., T. Plank, T. L. Grove, E. M. Stolper, S. Newman, and E. Hauri (2006), Mantle melting as a function of water content beneath back-arc basins, *J. Geophys. Res.*, *111*, B09208, doi:10.1029/2005JB003732.

Kennett, B. L. N., E. R. Engdahl, and R. Buland (1995), Constraints on seismic velocities in the Earth from travel-times, *Geophys. J. Int.*, *122*, 108–124, doi:10.1111/j.1365-246X.1995.tb03540.x.

Kent, A. J. R., D. W. Peate, S. Newman, E. M. Stolper, and J. A. Pearce (2002), Chlorine in submarine glasses from the Lau Basin: Seawater contamination and constraints on the composition of slab-derived fluids, *Earth Planet. Sci. Lett.*, *202*, 361–377, doi:10.1016/S0012-821X(02)00786-0.

Kilinc, A., I. S. E. Carmichael, M. L. Rivers, and R. O. Sack (1983), The ferric-ferrous ratio of natural silicate liquids equilibrated in air, *Contrib. Mineral. Petrol.*, *83*, 136–140, doi:10.1007/BF00373086.

Klein, E. M., and C. H. Langmuir (1987), Global correlations of ocean ridge basalt chemistry with axial depth and crustal thickness, *J. Geophys. Res.*, *92*, 8089–8115, doi:10.1029/JB092iB08p08089.

Langmuir, C. H., A. Bézos, S. Escrig, and S. W. Parman (2006), Chemical systematics and hydrous melting of the mantle in back-arc basins, in *Back-Arc Spreading Systems: Geological, Biological, Chemical and Physical Interactions*, *Geophys. Monogr. Ser.*, vol. 166, edited by D. M. Christie et al., pp. 87–146, AGU, Washington, D. C.

Lehnert, K., Y. Su, C. H. Langmuir, B. Sarbas, and U. Nohl (2000), A global geochemical database structure for rocks, *Geochem. Geophys. Geosyst.*, *1*(5), 1012, doi:10.1029/1999GC000026.

Le Maitre, R. W., et al. (1989), *A Classification of Igneous Rocks and Glossary of Terms*, 193 pp., Blackwell Sci., Oxford, U. K.

Martinez, F., and B. Taylor (2002), Mantle wedge control on back-arc crustal accretion, *Nature*, *416*, 417–420, doi:10.1038/416417a.

McDonough, W. F., and S.-S. Sun (1995), The composition of the Earth, *Chem. Geol.*, *120*, 223–253, doi:10.1016/0009-2541(94)00140-4.

Michael, P. J., and J. G. Schilling (1989), Chlorine in mid-ocean ridge magmas - Evidence for assimilation of seawater-influenced components, *Geochim. Cosmochim. Acta*, *53*, 3131–3143, doi:10.1016/0016-7037(89)90094-X.

Millen, D. W., and M. W. Hamburger (1998), Seismological evidence for tearing of the Pacific Plate at the northern termination of the Tonga subduction zone, *Geology*, *26*, 659–662, doi:10.1130/0091-7613(1998)026<0659: SEFTOT>2.3.CO;2.

Miller, D. M., S. L. Goldstein, and C. H. Langmuir (1994), Cerium lead and lead-isotope ratios in arc magmas and the enrichment of lead in the continents, *Nature*, *368*, 514–520, doi:10.1038/368514a0.

Miller, M. S., A. Gorbatov, and B. L. N. Kennett (2006), Three-dimensional visualization of a near-vertical slab tear beneath the southern Mariana arc, *Geochem. Geophys. Geosyst.*, *7*, Q06012, doi:10.1029/2005GC001110.

Nilsson, K., and C. L. Peach (1993), Sulfur speciation, oxidation-state, and sulfur concentration in backarc magmas, *Geochim. Cosmochim. Acta*, *57*, 3807–3813, doi:10.1016/0016-7037(93)90158-S.

Nilsson Farley, K. (1994), Oxidation state and sulfur concentrations in Lau Basin basalts, in *Proc. Ocean Drill. Program Sci. Results*, vol. 135, edited by J. Hawkins et al., pp. 603–613, Ocean Drill. Program, College Station, Tex.

Parkinson, I. J., and R. J. Arculus (1999), The redox state of subduction zones: Insights from arc-peridotites, *Chem. Geol.*, *160*, 409–423, doi:10.1016/S0009-2541(99)00110-2.

Peacock, S. M. (1996), Thermal and petrological structure of subduction zones, in *Subduction: Top to Bottom*, *Geophys. Monogr. Ser.*, vol. 96, edited by G. E. Bebout et al., pp. 119–133, AGU, Washington, D. C.

Pearce, J. A., and R. J. Stern (2006), Origin of back-arc basin magmas: Trace element and isotope perspectives, in *Back-Arc Spreading Systems: Geological, Biological, Chemical and Physical Interactions*, *Geophys. Monogr. Ser.*, vol. 166, edited by D. M. Christie et al., pp. 63–86, AGU, Washington, D. C.

Pearce, J. A., M. Ernewein, S. H. Bloomer, L. M. Parson, B. J. Murton, and L. E. Johnson (1995), Geochemistry of Lau Basin volcanic rocks: Influence of ridge segmentation and arc proximity, in *Volcanism Associated with Extension at Consuming Plate Margins*, edited by J. L. Smellie, *Geol. Soc. London Spec. Publ.*, *81*, 53–75.

Pearce, J. A., R. J. Stern, S. H. Bloomer, and P. Fryer (2005), Geochemical mapping of the Mariana arc-basin system: Implications for the nature and distribution of subduction components, *Geochem. Geophys. Geosyst.*, *6*, Q07006, doi:10.1029/2004GC000895.

Pearce, J. A., P. D. Kempton, and J. B. Gill (2007), Hf-Nd evidence for the origin and distribution of mantle domains in the SW Pacific, *Earth Planet. Sci. Lett.*, *260*, 98–114, doi:10.1016/j.epsl.2007.05.023.

Pearce, N. J. G., W. T. Perkins, J. A. Westgate, M. P. Gorton, S. E. Jackson, C. R. Neal, and S. P. Chenery (1997), A compilation of new and published major and trace element data for NIST SRM 610 and NIST SRM 612 glass reference materials, *Geostand. Newsl.*, *21*, 115–144, doi:10.1111/j.1751-908X.1997.tb00538.x.

Peate, D. W., T. F. Kokfelt, C. J. Hawkesworth, P. W. Van Calsteren, J. M. Hergt, and J. A. Pearce (2001), U-series isotope data on Lau Basin glasses: The role of subduction-related fluids during melt generation in back-arc basins, *J. Petrol.*, *42*, 1449–1470, doi:10.1093/petrology/42.8.1449.

Plank, T., and C. H. Langmuir (1998), The chemical composition of subducting sediment and its consequences for the crust and mantle, *Chem. Geol.*, *145*, 325–394, doi:10.1016/S0009-2541(97)00150-2.

Portnyagin, M., K. Hoernle, P. Plechov, N. Mironov, and S. Khubunaya (2007), Constraints on mantle melting and composition and nature of slab components in volcanic arcs from volatiles (H_2O, S, Cl, F) and trace elements in melt inclusions from the Kamtchatka Arc, *Earth Planet. Sci. Lett.*, *255*, 53–69, doi:10.1016/j.epsl.2006.12.005.

Reed, W. P. (1992), Certificates of analysis for SRMs 610–611; 612–613; 614–615; 616–617 (revised), Natl. Inst. of Stand. and Technol., Gaithersburg, Md.

Rietbrock, A., and C. Haberland (2001), A tear in the subducting Nazca Slab: Evidence from local earthquake tomography and high precision hypocenters, *Eos Trans. AGU*, *82*(47), Fall Meet. Suppl., Abstract T31A-0822.

Roeder, P. L., and R. F. Emslie (1970), Olivine-liquid equilibrium, *Contrib. Mineral. Petrol.*, *29*, 275–289, doi:10.1007/BF00371276.

Sakai, H., D. J. Desmarais, A. Ueda, and J. G. Moore (1984), Concentrations and isotope ratios of carbon, nitrogen and sulfur in ocean-floor basalts, *Geochim. Cosmochim. Acta*, *48*, 2433–2441, doi:10.1016/0016-7037(84)90295-3.

Saunders, A. D., and J. Tarney (1979), Geochemistry of basalts from back-arc spreading centre in the east Scotia Sea, *Geochim. Cosmochim. Acta*, *43*, 555–572, doi:10.1016/0016-7037(79)90165-0.

Scaillet, B., and B. Clemente (1998), Redox control on sulfur degassing in silicic magmas, *J. Geophys. Res.*, *103*, 23,937–23,949, doi:10.1029/98JB02301.

Sinton, J. M., L. L. Ford, B. Chappell, and M. T. McCulloch (2003), Magma genesis and mantle heterogeneity in the Manus back-arc basin, Papua New Guinea, *J. Petrol.*, *44*, 159–195, doi:10.1093/petrology/44.1.159.

Smith, I. E. M., and R. C. Price (2006), The Tonga-Kermadec arc and Havre-Lau back-arc system: Their role in the development of tectonic and magmatic models for the western Pacific, *J. Volcanol. Geotherm. Res.*, *156*, 315–331, doi:10.1016/j.jvolgeores.2006.03.006.

Stern, R. J., P. N. Lin, J. D. Morris, M. C. Jackson, P. Fryer, S. H. Bloomer, and E. Ito (1990), Enriched back-arc basin basalts from the northern Mariana Trough - Implications for the magmatic evolution of back-arc basins, *Earth Planet. Sci. Lett.*, *100*, 210–225, doi:10.1016/0012-821X(90)90186-2.

Stern, R. J., E. Kohut, S. H. Bloomer, M. Leybourne, M. Fouch, and J. Vervoort (2006), Subduction factory processes beneath the Guguan cross-chain, Mariana Arc: No role for sediments, are serpentinites important?, *Contrib. Mineral. Petrol.*, *151*, 202–221, doi:10.1007/s00410-005-0055-2.

Stoffers, P., et al. (2006), Submarine volcanoes and high-temperature hydrothermal venting on the Tonga arc, southwest Pacific, *Geology*, *34*, 453–456, doi:10.1130/G22227.1.

Stolper, E., and S. Newman (1994), The role of water in the petrogenesis of Mariana Trough magmas, *Earth Planet. Sci. Lett.*, *121*, 293–325, doi:10.1016/0012-821X(94)90074-4.

Stroncik, N. A., and K. M. Haase (2004), Chlorine in oceanic intraplate basalts: Constraints on mantle sources and recycling processes, *Geology*, *32*, 945–948, doi:10.1130/G21027.1.

Sun, S.-S., and W. F. McDonough (1989), Chemical and isotopic systematics of oceanic basalts: Implications for mantle composition and processes, in *Magmatism in the Ocean Basins*, edited by A. D. Saunders and M. J. Norry, *Geol. Soc. London Spec. Publ.*, *42*, 315–345.

Sun, W., V. C. Bennett, S. M. Eggins, R. J. Arculus, and M. R. Perfit (2003), Rhenium systematics in submarine MORB and back-arc basin glasses: Laser ablation ICP-MS results, *Chem. Geol.*, *196*, 259–281, doi:10.1016/S0009-2541(02)00416-3.

Syracuse, E. M., and G. A. Abers (2006), Global compilation of variations in slab depth beneath arc volcanoes and implications, *Geochem. Geophys. Geosyst.*, *7*, Q05017, doi:10.1029/2005GC001045.

Tatsumi, Y., and S. Eggins (1995), *Subduction Zone Magmatism*, 211 pp., Blackwell Sci., Oxford, U. K.

Taylor, B., and F. Martinez (2003), Back-arc basin basalt systematics, *Earth Planet. Sci. Lett.*, *210*, 481–497.

Toplis, M. J., and M. R. Carroll (1995), An experimental-study of the influence of oxygen fugacity on Fe-Ti oxide stability, phase-relations, and mineral-melt equilibria in ferro-basaltic systems, *J. Petrol.*, *36*, 1137–1170.

Turner, S., and C. Hawkesworth (1997), Constraints on flux rates and mantle dynamics beneath island arcs from Tonga-Kermadec lava geochemistry, *Nature*, *389*, 568–573, doi:10.1038/39257.

Turner, S., and C. Hawkesworth (1998), Using geochemistry to map mantle flow beneath the Lau Basin, *Geology*, *26*, 1019–1022, doi:10.1130/0091-7613(1998)026<1019:UGTMMF>2.3.CO;2.

Turner, S., C. Hawkesworth, N. Rogers, J. Bartlett, T. Worthington, J. Hergt, J. Pearce, and I. Smith (1997), U^{238}-Th^{230} disequilibria, magma petrogenesis, and flux rates beneath the depleted Tonga-Kermadec island arc, *Geochim. Cosmochim. Acta*, *61*, 4855–4884, doi:10.1016/S0016-7037(97)00281-0.

Van Der Hilst, R. D., S. Widiyantoro, and E. R. Engdahl (1997), Evidence for deep mantle circulation from global tomography, *Nature*, *386*, 578–584, doi:10.1038/386578a0.

Volpe, A. M., J. D. Macdougall, and J. W. Hawkins (1988), Lau Basin Basalts (LBB): Trace element and Sr-Nd isotopic evidence for heterogeneity in back-arc basin mantle, *Earth Planet. Sci. Lett.*, *90*, 174–186, doi:10.1016/0012-821X(88)90099-4.

Wallace, P. J. (2005), Volatiles in subduction zone magmas: Concentrations and fluxes based on melt inclusion and volcanic gas data, *J. Volcanol. Geotherm. Res.*, *140*, 217–240, doi:10.1016/j.jvolgeores.2004.07.023.

Wallace, P., and I. S. E. Carmichael (1992), Sulfur in basaltic magmas, *Geochim. Cosmochim. Acta*, *56*, 1863–1874, doi:10.1016/0016-7037(92)90316-B.

Weaver, J. S., and C. H. Langmuir (1990), Calculation of phase equilibrium in mineral-melt systems, *Comput. Geosci.*, *16*, 1–19, doi:10.1016/0098-3004(90)90074-4.

Wells, P. R. A. (1977), Pyroxene thermometry in simple and complex systems, *Contrib. Mineral. Petrol.*, *62*, 129–139, doi:10.1007/BF00372872.

Wendt, J. I., M. Regelous, K. D. Collerson, and A. Ewart (1997), Evidence for a contribution from two mantle plumes to island-arc lavas from northern Tonga, *Geology*, *25*, 611–614, doi:10.1130/0091-7613(1997)025<0611:EFACFT>2.3.CO;2.

Widiyantoro, S., B. L. N. Kennett, and R. D. Van Der Hilst (1999), Seismic tomography with *P* and *S* data reveals lateral variations in the rigidity of deep slabs, *Earth Planet. Sci. Lett.*, *173*, 91–100, doi:10.1016/S0012-821X(99)00216-2.

Wiens, D. A., K. A. Kelley, and T. Plank (2006), Mantle temperature variations beneath back-arc spreading centers inferred from seismology, petrology, and bathymetry, *Earth Planet. Sci. Lett.*, *248*, 30–42, doi:10.1016/j.epsl.2006.04.011.

Wright, D. J., S. H. Bloomer, C. J. MacLeod, B. Taylor, and A. M. Goodlife (2000), Bathymetry of the Tonga Trench and Forearc: A map series, *Mar. Geophys. Res.*, *21*, 489–511, doi:10.1023/A:1026514914220.

Wright, I. C., T. J. Worthington, and J. A. Gamble (2006), New multibeam mapping and geochemistry of the 30°–35°S sector, and overview, of southern Kermadec arc volcanism, *J. Volcanol. Geotherm. Res.*, *149*, 263–296, doi:10.1016/j.jvolgeores.2005.03.021.

Zellmer, K. E., and B. Taylor (2001), A three-plate kinematic model for Lau Basin opening, *Geochem. Geophys. Geosyst.*, *2*(5), 1020, doi:10.1029/2000GC000106.

Zhang, H. J., C. H. Thurber, D. Shelly, S. Ide, G. C. Beroza, and A. Hasegawa (2004), High-resolution subducting-slab structure beneath northern Honshu, Japan, revealed by double-difference tomography, *Geology*, *32*, 361–364, doi:10.1130/G20261.2.

Zhao, D. P., and J. R. Kayal (2000), Impact of seismic tomography on Earth sciences, *Curr. Sci.*, *79*, 1208–1214.

Zheng, Y. C., T. Lay, M. P. Flanagan, and Q. Williams (2007), Pervasive seismic wave reflectivity and metasomatism of the Tonga mantle wedge, *Science*, *316*, 855–859, doi:10.1126/science.1138074.

————————

R. J. Arculus and J. Hermann, Research School of Earth Sciences, Australian National University, Canberra, ACT 0200, Australia.

N. S. Keller, Geology and Geophysics Department, Woods Hole Oceanographic Institution, Woods Hole, MA 02543, USA. (nkeller@whoi.edu)

S. Richards, School of Earth Sciences, James Cook University, Townsville, Qld 4811, Australia.